UCRL 8302

UNIVERSITY OF
CALIFORNIA

Radiation
Laboratory

π^--p ELASTIC SCATTERING AND SINGLE PION PRODUCTION AT 0.939 Bev/c

BERKELEY, CALIFORNIA

DISCLAIMER

UCRL-8302
Physics and Mathematics

UNIVERSITY OF CALIFORNIA

Radiation Laboratory
Berkeley, California

Contract No. W-7405-eng-48

π^--p ELASTIC SCATTERING AND SINGLE PION PRODUCTION AT 0.939 Bev/c

Lee Baggett, Jr.

May 28, 1958

Submitted in partial fulfillment
of the requirements for the degree of

MASTER OF SCIENCE
IN
PHYSICS

United States Naval Postgraduate School
Monterey, California

Printed for the U. S. Atomic Energy Commission

π^--p ELASTIC SCATTERING AND SINGLE PION PRODUCTION AT 0.939 Bev/c

Contents

π^--p ELASTIC SCATTERING AND SINGLE PION PRODUCTION AT 0.939 Bev/c

Lee Baggett, Jr.

Radiation Laboratory
University of California
Berkeley, California

May 28, 1958

ABSTRACT

An investigation of π^--p elastic scattering and single-pion production at 0.939 Bev/c is reported. Five-hundred and forty two-prong interactions in the 10-inch UCRL liquid-hydrogen bubble chamber have been classified. Emphasis is given the methods used in the kinematic classification of events. The total cross section for π^--p interactions is found to be 53.3 ± 2.4 mb. The elastic-scattering cross section is 21.0 ± 1.1 mb. The elastic differential cross section displays a narrow diffraction peak in the forward direction. In the center-of-mass system, 35.6% of the elastic events have pion scatters into the backward hemisphere.

In single-pion production the ratio of the number of π^+ to π^0 productions is 2.49. The momentum distributions of the charged particles do not correspond to the phase-space distributions predicted.

π^- - p ELASTIC SCATTERING AND SINGLE PION PRODUCTION AT 0.939 Bev/c

Lee Baggett, Jr.

Radiation Laboratory
University of California
Berkeley, California

May 28, 1958

I. INTRODUCTION

An experimental study of elastic scattering and single-pion-production interactions of negative pions of 0.939 Bev/c momentum in hydrogen is reported here.

Pion-proton interactions in this Bev region leading to associated production have been investigated recently.[1,2,3] Inelastic pion reactions not involving "strange particles" have been neglected except for early, low-statistics experiments using diffusion cloud chambers[4,5] and nuclear emulsions.[6] Elastic pion-proton scattering in this energy region, on the other hand, has received additional treatment using a propane chamber[7] and, more recently, liquid hydrogen bubble chambers.[8]

The study described here is based on data obtained as a by-product of a recent associated-production experiment with the 10-inch hydrogen bubble chamber at the University of California Radiation Laboratory.[9] Approximately 600 two-prong pion events have been measured at each of three (nominal) beam momenta: 0.927, 1.12, and 1.24 Bev/c. The preliminary kinematic analysis of the 0.927-Bev/c data is reported here. Analysis of the 1.12- and 1.24-Bev/c momenta data will be reported later.

The following three reactions are considered:

$$\pi^- + p \rightarrow \pi^- + p,$$
$$\pi^- + p \rightarrow \pi^- + p + \pi^0,$$
$$\pi^- + p \rightarrow \pi^- + \pi^+ + n.$$

The decision to limit the kinematic analysis to the three listed reactions assumes that the frequency of events with the production of two or more secondary pions is negligible. The rarity of four-prong events,

$\pi^- + p \rightarrow \pi^- + p + \pi^+ + \pi^-$, supports this assumption. In principle, measurement of the charged-particle tracks in a magnetic field, and conservation of momentum and energy, determine unambiguously whether one or more neutral particles are involved. In practice the identification of missing neutral particles is made more difficult by measurement inaccuracies. Classification of multiple-pion-production events requires well-established criteria as to what constitutes a good kinematic fit in single-pion production. An approximate upper bound for multiple pion production will be established later.

This report treats the interpretation of the experimental results in only a cursory way. Specification of a single-pion-production event requires five intrinsic parameters, in contrast with the single center-of-mass scattering angle required for an elastic event. Consequently a detailed interpretive treatment of the data is relegated to the future. To keep the experiment in perspective, however, it is useful to list objectives of a study of elastic and single-pion-production events in this energy region.

a. Elastic π^--p scattering
   1. Determination of the size and opacity of the proton.
   2. Evaluation of the relative weights that the various angular-momentum states contribute to the interaction.
   3. Test of the validity of the dispersion relations (15% effect).
   4. Confirmation of the previously asserted backward-scattering peak (at higher energies).

b. Inelastic single-secondary-pion production
   1. Isotopic spin dependence of the interaction; the ratio of π^0 to n production (a priori of equal phase space).
   2. Evidence for the existence of a $T = J = \frac{3}{2}$ nucleon isobar.[10]
   3. Correlation of the inelastic pion production with associated production.

II. EXPERIMENTAL PROCEDURE

The π^--p interactions analyzed in this experiment were selected from a group of photographs taken in the 10-inch-diameter hydrogen bubble chamber. The chamber was provided with a 10,900-gauss magnetic field. Details of the hydrogen bubble chamber used have been described.[11] The exposure was the cooperative effort of the Alvarez group, and was primarily for the purpose of investigating associated production of strange particles at 0.927 Bev/c nominal beam momentum. The π^--beam trajectory is discussed elsewhere.[12] About 24,000 Bevatron pulses were photographed during the run. Approximately 4,800 of these were used in this analysis. All film was scanned by the professional scanning staff.

III. SCANNING EFFICIENCY AND ACCEPTANCE CRITERIA

A. Scanning Efficiency

1. General

At each transit of the π^- beam through the bubble chamber, two stereophotographs of the chamber were taken. After processing, the 35-mm film was scanned for all events of interest. Pion interactions were recorded, according to frame number and type, by means of check marks in appropriate columns of the scan sheets. Events entered on these scan sheets were subsequently examined in detail, sketched, and measured. The 13 rolls of film used in this experiment were scanned twice. Several factors which reduce the probability of seeing an event are discussed, together with their compensating corrections.

2. Depth Dependence

An event with its vertex near the top or bottom glass plates of the chamber is likely to be missed because one or both of the emergent prongs can be very short. An analysis of this chamber depth dependence was based on a comparison of the vertical distribution of 575 event vertices and the vertical distribution of 1126 beam tracks. The chamber was considered as divided into five horizontal regions. The median

plane of the central region, C, coincides with the median plane of the bubble chamber; depth of region C is 3.2 in. Regions A and E are the extreme regions, extending to the top and bottom glasses, respectively. Regions B and D lie between the central region and regions A and E, respectively. These divisions are each 0.8 in. in depth.

The depths of beam tracks in every 50th frame were measured. The vertical position of each event vertex was obtained by measurement on the precision measuring engine. The ratio of event density to track density within each horizontal section of the chamber is a measure of scanning efficiency within that region. These ratios are as follows.

Table I

Chamber Depth Dependence

Region	Events(N)	Beam Tracks(M)	Ratio (N/M)
A	2	2	$1.00^{+4.80}_{-0.83}$
B	3	12	$0.25^{+0.30}_{-0.17}$
C	563	1082	$0.52^{+0.04}_{-0.04}$
D	6	22	$0.27^{+0.22}_{-0.14}$
E	1	8	$0.12^{+0.27}_{-0.12}$
Total	575	1126	0.51

Obviously scanning efficiency for events in depth region E is poor. The ratios for all other regions agree within statistics, and only the events found in these four regions were considered. No correction to scanning efficiency as a function of chamber depth was made.

3. x-y Dependence

A reaction that occurs near the chamber wall may also be difficult to detect because of short tracks. Aside from this consideration, momentum and angle measurements become less accurate as the length of track available for measurement decreases. Hence, long tracks

were desired. A central area was superimposed on one stereo view at the stereo projector, using chamber fiducials for positioning; only those events whose vertices projected into the area were considered for measurement. This criterion not only increased the scanning efficiency, and the probability of having long tracks, but it also made identification of events from the decay, interaction, or stopping of one of the emergent prongs more likely.

In order to detect any variation in scanning efficiency within the acceptance area, this area was divided into five equal regions, as shown in Fig. 1. The distribution of 600 projected vertex positions was compared with the distribution of 8562 beam tracks crossing the area. All tracks in every tenth frame of the experiment were counted. On the histogram of beam track distribution, Fig. 2, the number of events within each subdivision of the acceptance area has been indicated. The ratio of event density to track density within each region of the acceptance area is a measure of the scanning efficiency for events within that region. These ratios are as follows.

Table II

x-y Dependence

Region	Events(N)	Beam Tracks(M)	Ratio(N/M)
1	91	1415	0.064 ± .009
2	122	1784	0.068 ± .008
3	152	2115	0.072 ± .007
4	141	1871	0.075 ± .009
5	94	1377	0.068 ± .009
Total	600	8562	0.070

These ratios indicate that scanning efficiency is uniform, within statistical accuracy, throughout the acceptance area, and that no dependence of scanning efficiency on position in this area need be considered.

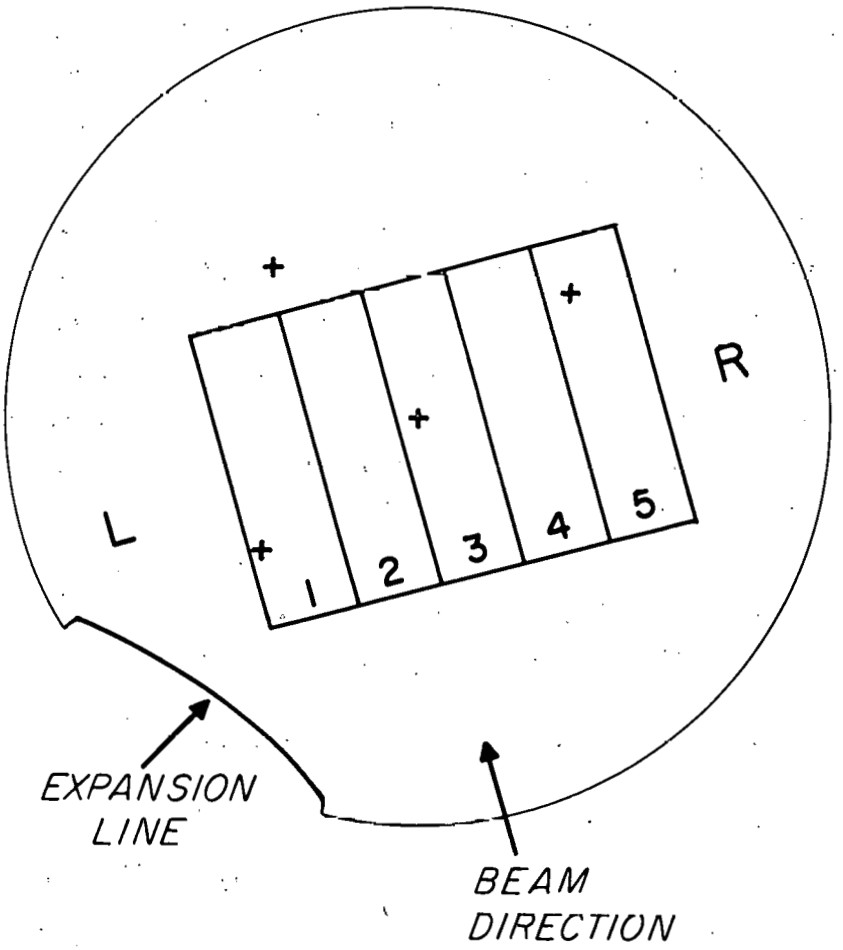

Fig. 1. Projected view of bubble chamber, showing acceptance area.

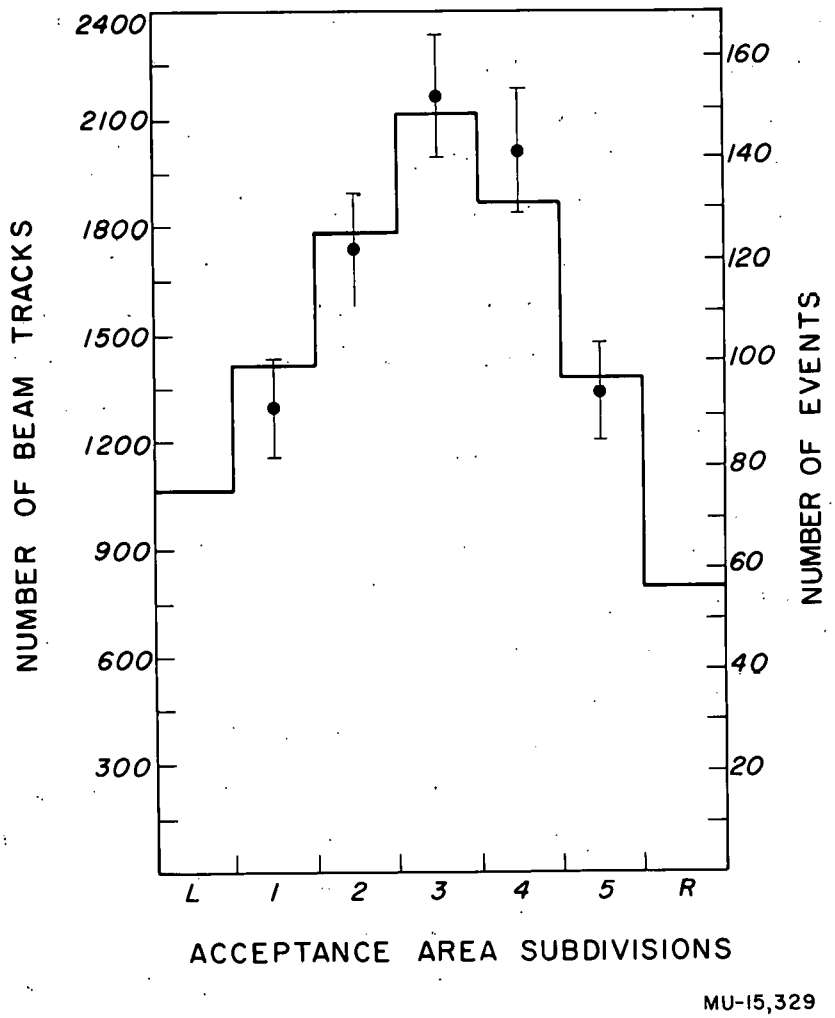

Fig. 2. Projected x-y distributions within acceptance region. Histogram of distribution of 8562 beam tracks. (600 events)

4. Orientation of Outgoing Prongs

Events that have one or both prongs near the vertical are more likely to be overlooked than events with prongs more nearly horizontal. To study the dependence of scanning efficiency on orientation of the plane defined by the two prongs, a plot of the number of events as a function of the angle Φ was constructed. Here Φ is the angle between the horizontal plane and the plane containing the two prongs. This plot is shown in Fig. 3. The scattering should be isotropic in Φ, and the anisotropy observed is a measure of the dependence of scanning efficiency on event orientation. A correction factor of $1.18 \pm .03$ is derived from the data illustrated in Fig. 3. The total number of events seen must be multiplied by this correction factor to account for the scanning-efficiency dependence on Φ.

5. Repeated Scans

All film used in this experiment was scanned twice by two independent observers. Within the acceptance volume there were 922 events seen by both observers; 33 events were seen by the first scanner but not seen by the second; 27 events were seen by the second scanner but not by the first. The indicated efficiency of each scanner is $97\% \pm 1\%$. The total number of observable two-prong events, based on these scans, is 983 ± 1. The total number of two-prong events, after correction for scanning-efficiency dependence on Φ, is 1160 ± 31.

B. Acceptance Criteria

Each two-prong event within the acceptance area was examined at a scanning table before being measured. Acceptance criteria, specified to reduce analysis time and measurement errors, and to fully utilize the automatic tracking capability of the measuring engine, were imposed on each event. These criteria were: (1) The vertex was distinct, i.e., no track not associated with the event fell within one track width of the vertex in either projected view. (2) The incident track direction was within 3° of the mean incident beam direction. (3) The incident track curvature was approximately the same as the mean beam curvature. (4) Not more than thirty beam tracks were visible in either view.

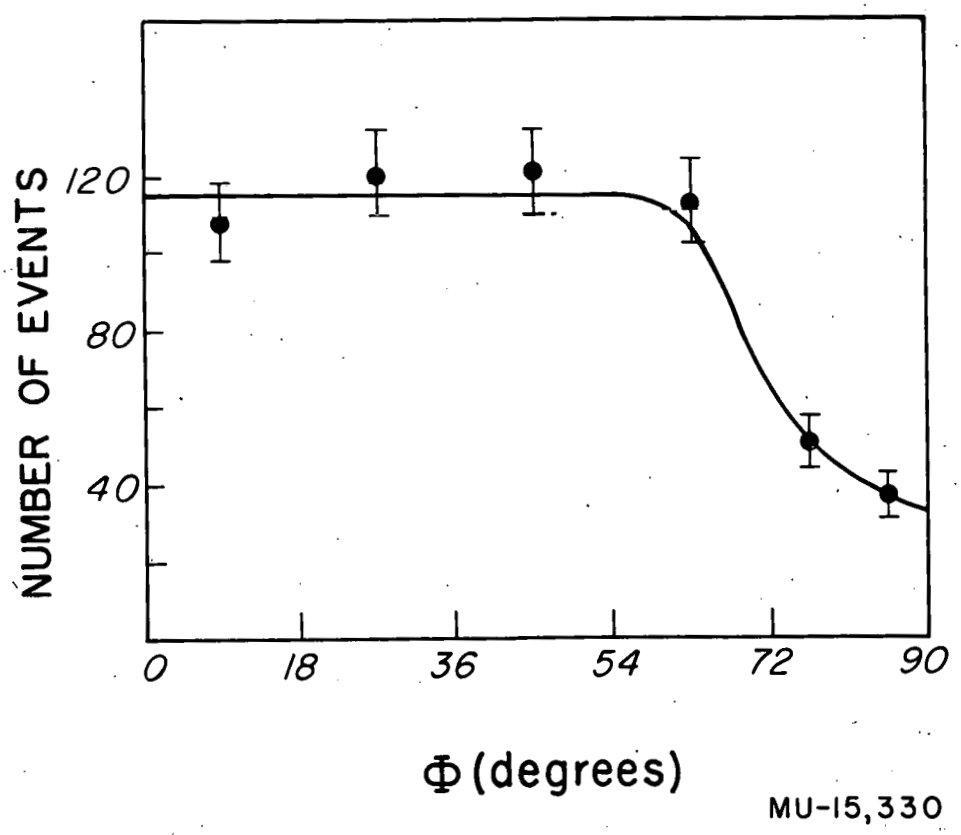

Fig. 3. Orientation of plane of emergent prongs. Folded distribution of 550 events. $\Phi = 0^{o} \equiv$ flat in chamber.

IV. TRACK ANALYSIS

A. Spatial Reconstruction of a Track

Each of the two views of an event accepted for measurement was projected on the screen of the precision measuring engine (Franckenstein). This servo auto-tracking projector takes a series of points along each prong of the event in each of the two stereo views. The solution of the optical problem and the determination of a set of points in chamber space from the Franckenstein measurements have been previously described.[11]

When the space coördinates x_i, y_i, z_i ($i = 1, 2, \cdots, n$) for each of the n measured points along a track have been determined, a least-squares fit of a parabola is made to the projection of these points on the x-y plane. (Fig. 4.) The least-squares fit is made on the x_i'' and y_i'' points following a translation and rotation to the x", y" coördinates used to simplify the scaling problem for the digital computer. The x", y" coördinates are fitted to the parabola

$$y_i'' = a + b\, x_i'' + c\, x_i'' .$$

(The event reconstruction described is programmed for the IBM-650 computer.)

Although the projection of the track on the x-y plane is a circular arc, a parabolic fit is made rather than a fit to a higher-order curve, because at the momenta measured the increase in accuracy is not sufficient to justify more elaborate programming.

When the parabola has been determined, the root-mean-square deviation σ_{xy} of the measured points from the fitted curve is expressed by

$$\sigma_{xy} = \left(\frac{\sum_1^n \delta_i^2}{n-3} \right)^{\frac{1}{2}} ,$$

where n is the number of points measured, and δ_i is the deviation of each projected point from the fitted curve. For $n \leq 3$, σ_{xy} is not meaningful, since a parabola can be fitted exactly to three points, and therefore no calculation of σ_{xy} is made.

The azimuthal angle, between the tangent to the x-y projection of the track and the x axis, is given by $\phi = \theta_R + \theta^{LS}$. The value of θ^{LS} is obtained from the coefficients b' and c' and the half-chord

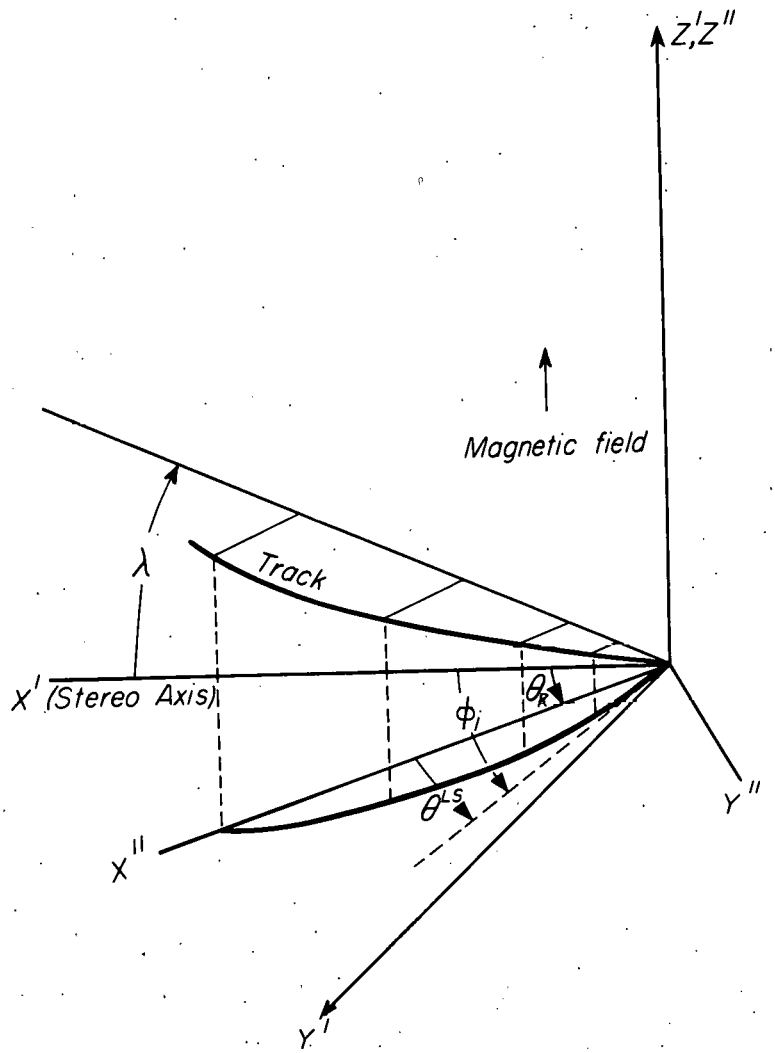

Fig. 4. Space coördinate system and track projections into planes.

length R:

$$R = \bar{x}'' - x_1''.$$

For each track there are two azimuthal angles, ϕ_i and ϕ_f, corresponding respectively to the beginning and end of each track. The value ϕ_f is used only with the incident beam track, for on this track alone is measurement directed toward the event vertex.

To specify the length of the track, ℓ, and the dip angle λ, the coördinates are fitted to a straight line in the x''-z'' plane. Although it is true that each track is a helix, and hence its projection on the x''- z'' plane is sinusoidal, the momenta were sufficiently high to allow a least-squares fit to be made to the straight line $z_i'' = d + ex_i''$. The root-mean-square deviation, defined by

$$\sigma_Z = \left(\frac{\sum_1^n \delta_i^2}{n-2} \right)^{\frac{1}{2}},$$

is then obtained from the coefficients of the straight-line expression. As above, δ_i and n are the deviations of the measured points (projected into the x''z'' plane) from the fitted curve and the number of points measured, respectively.

With the z dependence of the track now specified, the dip angle λ and the track length ℓ are given by the expressions

$$\tan \lambda = - \frac{e}{R}; \quad \ell = 2(e^2 + R^2)^{\frac{1}{2}}.$$

Fitted end points are obtained from the least-squares solution.

The final quantity of interest--the projected curvature of the track K--is determined from the fit in the x-y plane, according to $K = 1/.3H\rho$, where $\rho = R^2/2c$. The magnetic field strength, H, is evaluated at the midpoint of the track. The momentum can be calculated from the curvature K and dip angle λ by the expression $p = (K \cos \lambda)^{-1}$.

B. Measurement Errors

The automatic tracking feature of the precision measurement projector makes positioning of the stage at each point operator-independent. This feature makes it feasible to accurately determine the errors associated with measurements of angle and curvature.

Semi-empirical formulae for the standard deviation errors in the curvature K of a track, the azimuthal angle ϕ, and the tangent of the dip angle, $\tan\lambda$, were constructed from statistical studies of measurements made both on beam tracks and on tracks of actual events.

Errors fall into two categories: (a) internal-measurement errors, which reflect the accuracy of the measuring device and the intrinsic image quality of track; (b) turbulence errors, resulting from distortion of tracks by the turbulent liquid hydrogen during the time interval between occurrence of the event and the light flash.

1. Internal Measurement Errors

During measurement, track points are taken at approximately 1-centimeter intervals along the projection of the track in the x-y plane. A fit to these measured points $(x_j, y_j; j = 0, 1, \cdots n)$, assuming equal standard deviations for the y setting for all points, is specified as follows: the χ^2 quantity,

$$\chi^2 = \frac{1}{\sigma^2} \sum_{j=0}^{n} \left(y_j - \sum_{i=0}^{m} a_i x_j^i \right)^2 ,$$

is required to assume a minimum value for the "best" trial value of the parameters $a_i (i = 0, 1, \cdots m)$. The intrinsic accuracy of the a_i, once determined, leads directly to the standard deviations σ_K', σ_ϕ', and $\sigma'_{\tan\lambda}$ attributive to measurement technique.

Let us consider the error in the dip tangent. If the z dependence of a track is stated as $z = a_0 + a_1 x$, with x the distance along the projected chord length of the track, the dip tangent is given by $\tan\lambda = dz/dx = a_1$. The standard deviation is then

$$\sigma'_{\tan\lambda} = \sigma_{a_1}$$

or

$$\sigma'_{\tan\lambda} \cong \frac{\sqrt{3}}{R}\frac{\sigma_Z}{\sqrt{N}} C_N^{\lambda}, \qquad \text{(IV-1)}$$

where R is one-half the projected chord length, N is the number of points measured, and C_N is a correction factor for dependence on the number of points taken.[13]

The derivation of error in azimuthal angle follows a similar pattern. When a fit has been obtained in the x-y plane of the chamber, following coördinate rotation, of the form

$$y = a_0 + a_1 x + a_2 x^2,$$

then examination of Fig. 4 shows:

$$\tan(\phi_i - \phi_R) = dy/dx\big|_{x=0} = a_1.$$

For a 10-cm track with momentum of 150 Mev/c, $\phi_i - \phi_R = 14.7^{\circ}$, and this angle decreases rapidly with increasing momentum. Setting $\cos(\phi_i - \phi_R) = 1$ allows the error in ϕ_i to be written[13]

$$\sigma'_{\phi} \cong \frac{4\sqrt{3}}{R\sqrt{N}} \sigma_{xy} C_N^{\phi}. \qquad \text{(IV-2)}$$

On the basis of the equation for the fitted curve, as given above, the curvature of a track can be defined as

$$K = (d^2y/dx^2)\,[1 + (dy/dx)^2]^{-3/2}.$$

Evaluation of this expression at $x = R$ gives $K = 2\,a_2$, where, by choice of coördinate axes, the $(dy/dx)^2$ contribution can be neglected. Propagating the error of fit in a, one can approximate the curvature error[13] by

$$\sigma'_K \cong \frac{3\sqrt{5}}{R^2\sqrt{N}} \sigma_{xy} C_N^{K}. \qquad \text{(IV-3)}$$

Both σ_{xy} and σ_Z are calculated for the fit achieved. From repeated measurements of individual events and measurements of

beam tracks, mean values of 0.0041 cm and 0.0558 cm, respectively, were found. Use of these σ_{xy} and σ_z with Eqs. (IV-1) to (IV-3), B = 305 cm/Bev/c where B = 1/(pK), based on the mean 10.9-kilogauss magnetic field, results in the following approximate expressions for internal measurement errors:

$$\sigma'_{\tan\lambda} \cong \frac{0.3}{R\sqrt{N}} [1 + 2|\sin\phi|]^{-1}[1 - 0.76/N], \qquad (IV-4)$$

$$\sigma'_{\phi} \cong \frac{1.54}{R\sqrt{N}} [1 - 1/N], \qquad (IV-5)$$

$$\sigma'_{K} \cong \frac{8.30}{R^2\sqrt{N}} \left[1 - \frac{2.2}{N}\right]. \qquad (IV-6)$$

The ϕ dependence of $\sigma_{\tan\lambda}$ reflects the use of both stereographic views in the determination of $\tan\lambda$.

2. Turbulence Errors

The superheated condition required for track formation is obtained by rapid expansion of the liquid hydrogen prior to entry of each beam pulse. Because of turbulence following each expansion, tracks in the chamber are distorted, and curvatures obtained from photographs of these tracks can differ considerably from the curvatures of the actual ionizing particles.

The momentum-error data of Cresti[14] were taken as the basis for including turbulence effects within the total curvature error, σ_K. Measurements of 386 beam tracks at 1.12 Bev/c momenta were made. The square of the standard deviation of curvature can be expressed as

$$\sigma_K^2 = \frac{1}{N-1} \sum_{i=1}^{N} \left[\frac{1}{p_i} - \left(\frac{1}{p}\right)_{mean}\right]^2, \qquad (IV-7)$$

where $(1/p)_{mean}$ is the mean value of measured curvatures. Data were obtained by Cresti under the following conditions: (a) photographs were taken with 3 msec. light delay; (b) tracks were in the central region of the chamber (the exact form of turbulence is dependent on the position of the track with respect to the chamber expansion line);

(c) the average interval between measured points was 1.0 cm. Measurements were made on beam-track segments of varying lengths; three average track lengths were used to determine the R dependence of σ_K^2. The average lengths of the tracks considered were 6.1, 9.8, and 19.8 cm. The three points of Fig. 5 were determined by use of Eq. (IV-7) and the Cresti measurements.

A fit of these points is possible with a quadratic expression $\sigma_K^2 \sim A + Bx + Cx^2$, where $x = R^{-2}$ and R, the half chord length of the projected arc. Such a fit is indicated by inspection of the points. The correspondence between the functional form of the internal error in curvature, σ_K' in Eq. (IV-6), and the last term of this expression made possible a natural division of the total error, i.e., $\sigma_K^2 = (\sigma_K'')^2 + (\sigma_K')^2$, where σ_K'' and σ_K' are the turbulence and internal-measurement errors respectively. The dependence of C' on N, the number of points measured on a track, was taken from the internal-error expression as $C(N) \cong \frac{C'}{N}(1 - \frac{1.5}{N})$. For flat tracks with points taken at 1.0-cm intervals, one has $N \cong 2R$, hence the expression

$$\sigma_K^2 = A + BR^{-2} + 0.5\, C'\, R^{-4}[R^{-1}(1 - 0.75\, R^{-1})] \quad \text{(IV-8)}$$

was fitted to the points indicated. The coefficients A, B, and C' required for this fit were

$$A = 9.32 \times 10^{-3}, \qquad B = 0.174, \qquad C' = 62.5.$$

Repeated measurements of single events were also used to distinguish between internal errors and turbulence errors.

In the kinematic analysis of events, Section V, the quantity ξ_i/σ_{ξ_i}, where $\xi_i = (x_i - x_i^m)/\sigma_i$, $(i = 1, 2, \cdots 9)$, is a measure of the shift made in the ith variable to obtain a fit to a designated interpretation. The distributions of ξ_2/σ_{ξ_2} and ξ_3/σ_{ξ_3} over a number of different events are a measure of the fidelity of the total-curvature error formulae when applied to the outgoing negative and positive track respectively. Histograms of these distributions are shown in Fig. 6.

The distributions of ξ_i/σ_{ξ_i} over many different events complement the repeated-measurement technique, and these distributions were used in the adjustment of the error-formulae coefficients.

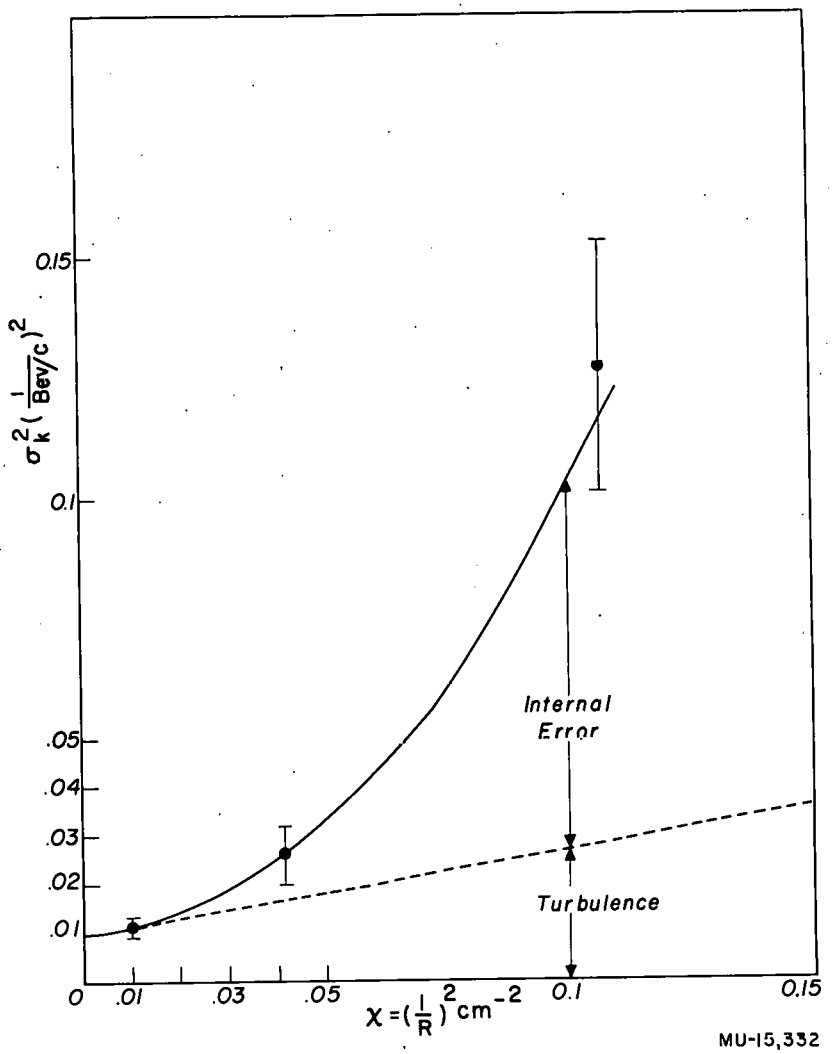

Fig. 5. Curvature error from study of 386 beam tracks.

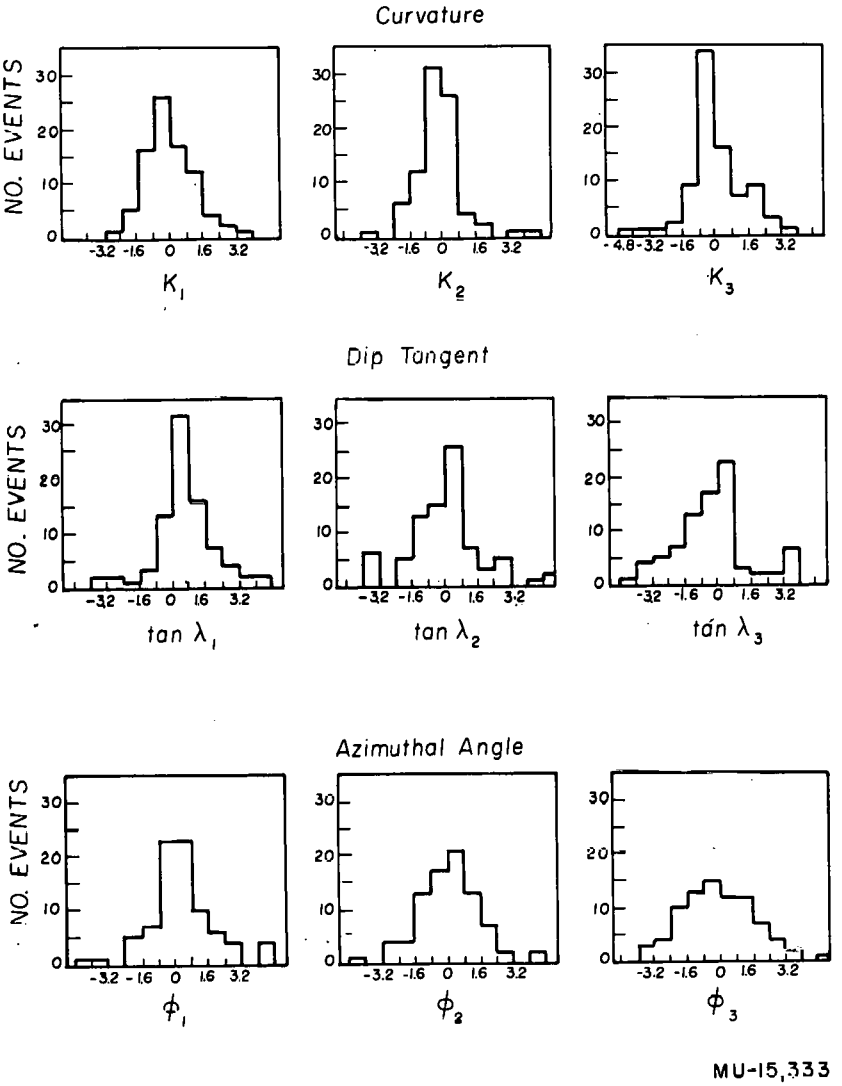

Fig. 6. ξ_i/σ_{ξ_i}, normalized adjustment of variables, 84 elastic events (with stopping proton).

The error formulae as programmed for normal nonstopping tracks are

$$\sigma_K = [A + B/R^2 + C/R^4]^{\frac{1}{2}} \quad (\text{Bev/c})^{-1} \qquad \text{(IV-9)}$$

where

$A = 18.64 \times 10^{-3}$,

$B = 0.226$,

$C = (62.5/N)(1 - 1.5\ N^{-1})$,

$R = \frac{1}{2}$ projected chord length (cm),

N = number of points measured in View I;

$$\sigma_\phi = [\sigma'^2_\phi + \sigma''^2_\phi]^{\frac{1}{2}} \quad \text{(degrees)} \qquad \text{(IV-10)}$$

where

$$\sigma'^2_\phi = 1.85\ R^{-1}\ N^{-\frac{1}{2}}\ [1 - 1/N],$$

$$\sigma''^2_\phi = (0.188\,R)^2\ (A + B/R^2);$$

and

$$\sigma_{\tan\lambda} = \frac{0.4}{RN^{\frac{1}{2}}}\ (1 + 2\,|\sin\phi|). \qquad \text{(IV-11)}$$

The σ''_ϕ term in Eq. (IV-10) reflects the effect of turbulence on azimuthal angle ϕ. It can be shown that this turbulence error, σ''_ϕ, and the turbulence error in curvature, σ''_K, are related by the expression

$$\sigma''_\phi(\text{rad.}) = (R/305)\sigma''_K,$$

where 305 cm/(Bev/c) relates curvature and momentum in the magnetic field, and $\sigma''_K = (A + B/R^2)^{\frac{1}{2}}$, as specified in Eq. (IV-9).

For protons that stopped in the chamber, the momentum (and hence the curvature) was determined from the range-momentum formula, $p = 0.141\,\ell^{0.273}$, where ℓ is track length (cm). This expression, based on the range-momentum curves for liquid hydrogen,[11] defines the proton momentum much more accurately than is possible when curvature measurements are based on parabolic fittings.

The range-momentum expression can be approximated by $p \cong 0.141\, \ell^{\frac{1}{4}}$ for determination of curvature error associated with measurement of a stopping proton. With half projected chord length, R, and dip-angle tangent, $\tan\lambda$, as independent variables, differentiation of this expression gives

$$\sigma_p \cong \frac{1}{4K}\left[\left(\frac{\sigma_R}{R\cos\lambda}\right)^2 + (\sin\lambda\ \sigma_{\tan\lambda})^2\right]^{\frac{1}{2}}, \qquad \text{(Bev/c)},$$

where $\ell = 2R/\cos\lambda$. For "flat" tracks this expression reduces to $\sigma_K \cong K\sigma_R/4R$. A value of 0.055 cm was taken as the error in one-half chord length, σ_R. This value was the standard deviation in range for 444 μ^+ ranges measured by Clark and Diehl,[11] using the same measuring engine. The approximation programmed was

$$\sigma_K \cong 0.014\ K/R, \qquad (\text{Bev/c})^{-1} \qquad \text{(IV-12)}$$

Since the error in K for stopping protons is essentially internal-measurement error, 36 remeasurements of event No. 495,621 were made to test this approximation. The arithmetic mean of the 36 σ_K's for the stopping proton obtained by Eq. (IV-12) was 0.072 $(\text{Bev/c})^{-1}$. The K_3 distribution for these remeasurements, shown in Fig. 7, has a standard deviation of 0.128 $(\text{Bev/c})^{-1}$. The disagreement between the calculated error and the error associated with a typical event indicates the dependence of range-measurement accuracy on track characteristics. The measurements by Clark and Diehl were restricted to flat tracks with angles of intersection--at the vertex--between 30° and 150°, and to the less heavily ionizing muon and electron tracks--that is, conditions not normally encountered with actual recoil protons. These considerations suggested that the expression for error in K be broadened to

$$\sigma_K \cong 0.024\ K/R. \quad (\text{Bev/c})^{-1} \qquad \text{(IV-13)}$$

The typical accuracies of the two methods of measuring curvatures (momenta) are illustrated by event No. 494,808:

track length (ℓ) = 3.034 cm.;

$\lambda = 58.59^\circ$;

momentum by curve fitting, p_c = 121.3 Mev/c;

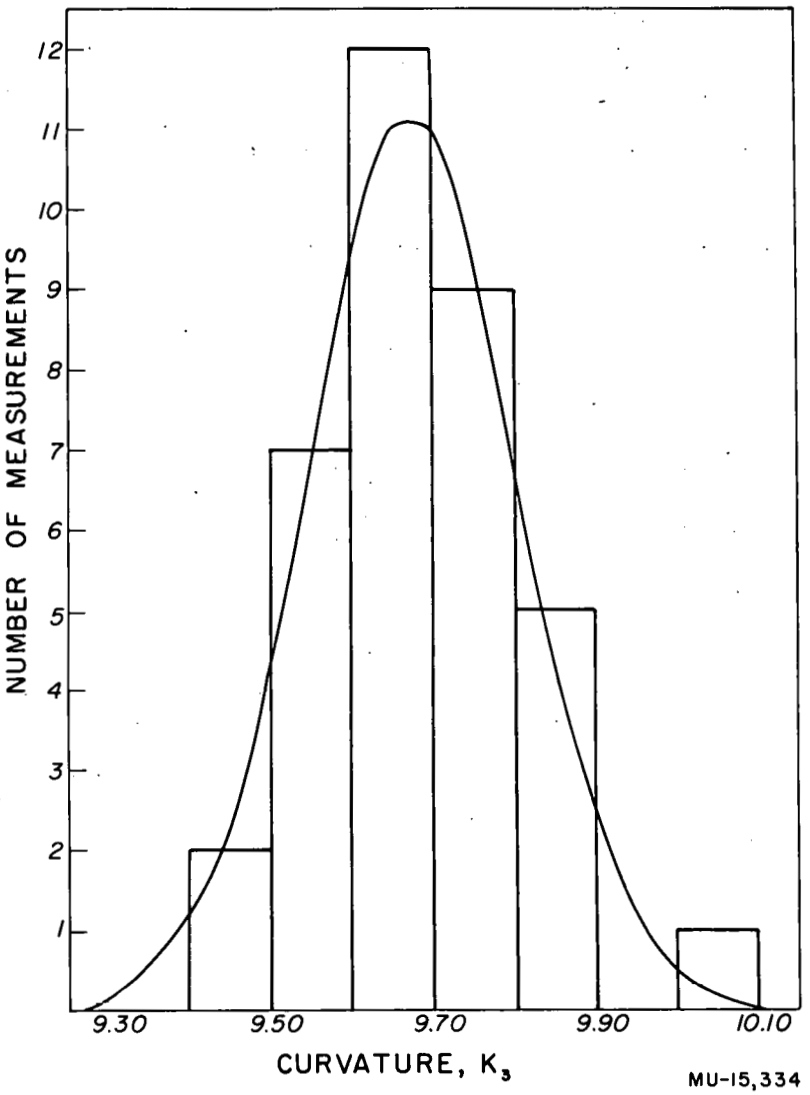

Fig. 7. Curvature of stopping proton; 36 repeated measurements of event No. 495,621. $\overline{K}_3$ = 9.68/Bev/c; σ_{K_3} = 0.128/Bev/c.

momentum from range, p_r = 192.2 Mev/c;

momentum from least-squares adjustment, p_f = 188.5 Mev/c;

momentum-measurement error from σ_K, Eq. (IV-13), σ_p = 5.0 Mev/c.

Here p_r and p_c differ from p_f, the "best" value of the momentum, by 2% and 36%, respectively. The adjustment of p_r to obtain a "fit" was 0.74 σ_p. The inaccuracy of p_c reflects the short projected length of track (1.63 cm) available for the parabolic fitting.

3. Incident-Beam Momentum

The nominal beam momentum of 0.927 Bev/c was determined from a study of pion trajectories through the collimation system.[12] The absolute value of the mean pion-beam momentum was determined from an analysis of 77 elastic events in which the proton stopped in the chamber. The nominal beam momentum, with a standard deviation of 0.278 Bev/c, was used in the kinematic fit program discussed in Section V. This large, unrealistic error allowed unrestricted shifting of the beam curvature, K_1, in obtaining a fit to the intrepretation. In effect, no exact beam momentum was assumed. The adjustment parameter

$$\xi_1 = \frac{x_1 - x_1^M}{\sigma_1} \quad ,$$

where x_1 and x_1^M are respectively "best fit" and nominal values of K_1, and $\sigma_1 = \sigma_{K_1} \sim 0.278$ Bev/c, indicates the adjustment of K_1 required for each event to fit the interpretation. The ξ_1 histogram for the 77 events is given in Fig. 8. The mean ξ_1 of -0.0414 ± .005 corresponds to a mean beam momentum adjustment to 0.939 ± .006 Bev/c. The mean beam momentum, from a study of three associated production events of the type $\pi^- + p \rightarrow \Lambda + K^0$ and $\pi^- + p \rightarrow V^0$ obtained during this exposure, gives p_1 = 0.938 ± .002 Bev/c.[15] A beam momentum p_1 = 0.939 ± .007 Bev/c was used. The indicated beam spread, ± 0.007 Bev/c, is supported by a detailed study of associated production at 1.12 Bev/c.[15] The beam trajectories through the magnetic steering magnets and through the collimation system were in all essentials identical with the 0.927-Bev/c experimental setup. The study of stopping protons, on the other hand, indicated only that the beam spread was less than ± 0.035 Bev/c, a width that reflects the large intrinsic measurement error of the method.

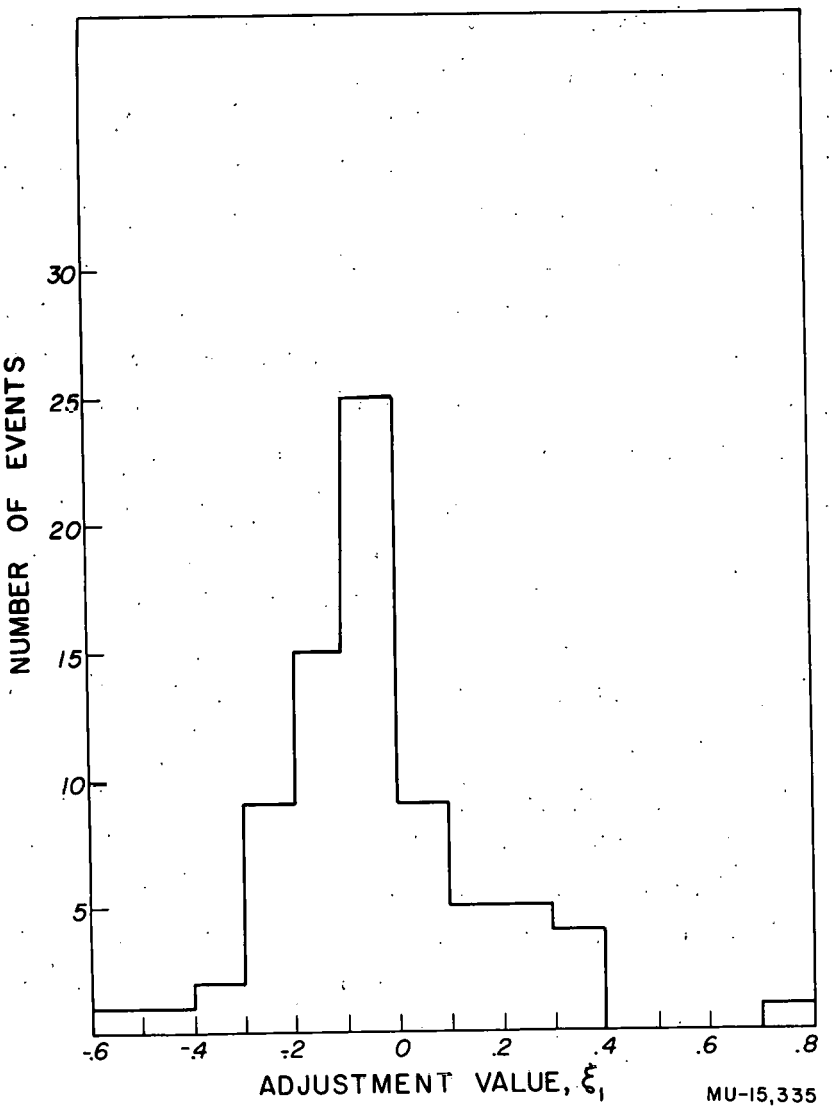

Fig. 8. Adjustment of beam curvature for least-squares fit. Mean ξ_1 = -0.414 ± .005; σ_{ξ_1} = 0.1727.

V. KINEMATIC ANALYSIS

A. General

In the past, it was possible for the physicists using cloud chambers to keep up with the data accumulation by "hand analysis" techniques. The bubble chamber, with its relatively high density, has greatly increased the number of interesting events observed, and therefore has stimulated the development of rapid analysis techniques. In this experiment an event was observed with approximately one out of every two Bevatron pulses, or 300 events were photographed each hour. The analysis of the events photographed during one 24-hour period of operation would require several man-years of "hand analysis." Rapid precision analysis techniques are obviously required if the rate of analysis is to parallel the accumulation of data.

All computations described in this report were carried out by use of the IBM type 650 digital computer. The procedure followed in the analysis of two-prong events is outlined in Fig. 9. The measurement and event-reconstruction phases of analysis have been discussed in Section IV.

B. Computation of Measurement Errors and Coplanarity

The origin of measurement errors and the derivation of requisite formulae are discussed in Section IV. The computer is programmed to calculate the errors associated with all angle and curvature measurements. A section of this program computes the included angle between any two tracks; individual track errors are propagated to these included angles.

The coplanarity of an event may be measured by the value of $R = \hat{n}_1 \cdot (\hat{n}_2 \times \hat{n}_3)$, where $\hat{n}_1$, $\hat{n}_2$, $\hat{n}_3$ are the unit vectors in the direction of the incident π^- and the two outgoing prongs, respectively, at the vertex. Perfect coplanarity is, of course, indicated by $R = 0$; however, because of measurement errors, events that are actually coplanar may have values of $R \neq 0$. A coplanarity function F and its associated error, σ_F, were used in establishing the degree of coplanarity of each event. Here R and F are related by

$$R = F \cos\lambda_1 \cos\lambda_2 \cos\lambda_3,$$

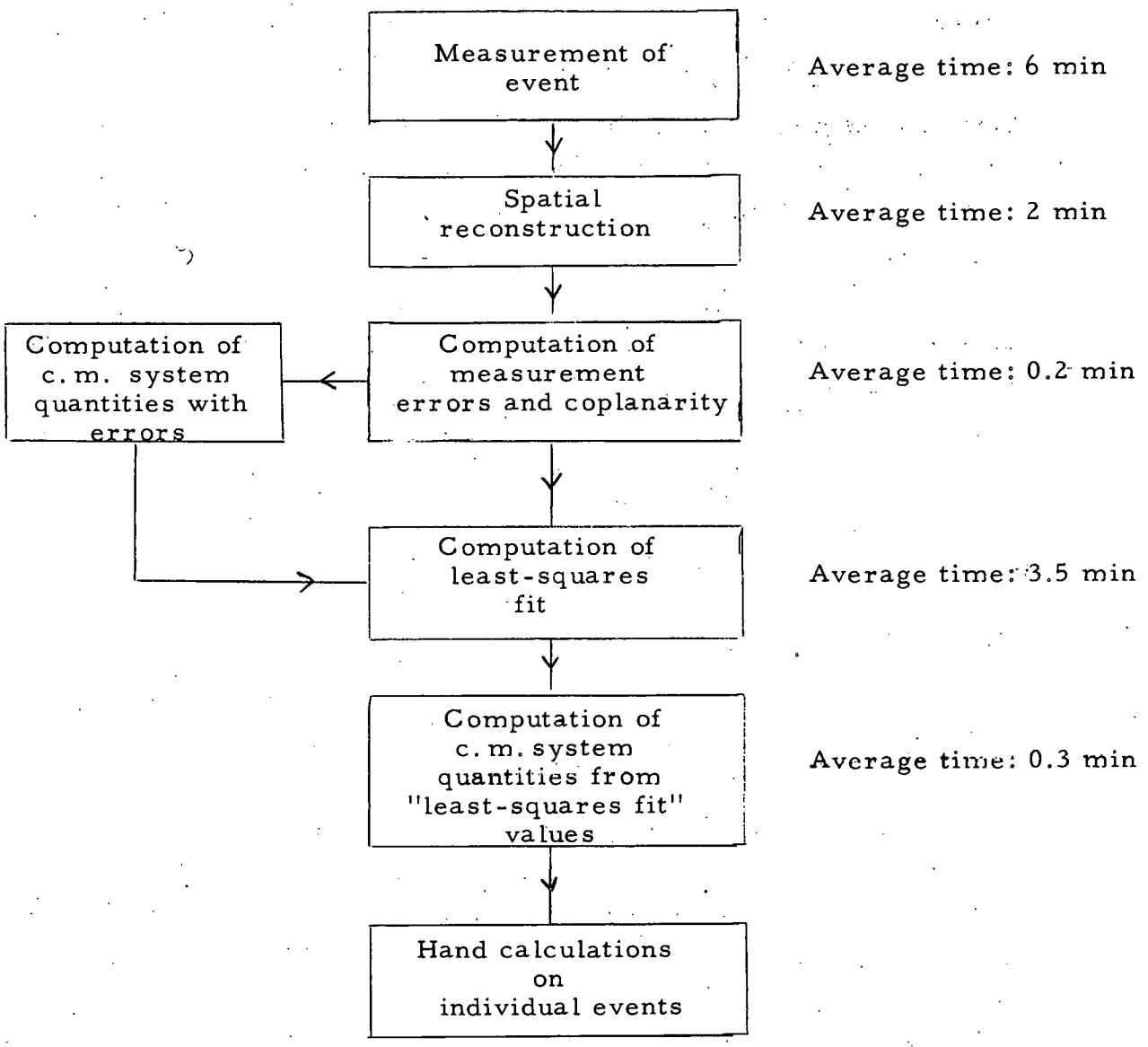

Fig. 9. Flow diagram for analysis of two-prong event; computer time indicated.

where

$$F = \tan\lambda_1 \sin(\phi_2-\phi_3) + \tan\lambda_2 \sin(\phi_3-\phi_1) + \tan\lambda_3 \sin(\phi_1-\phi_2).$$

Since tracks dipping or rising vertically in the chamber are not seen, $\cos\lambda$ is never zero, and $R = 0$ if and only if $F = 0$. The error, σ_F, is determined directly from the measurement errors computed for each track. The quantity $|F|/\sigma_F$ indicates coplanarity within measurement errors. Figure 10 is a histogram of $|F|/\sigma_F$ values for elastic and inelastic events. For the inelastic events a broad distribution of $|F|/\sigma_F$ is expected, since the lack of coplanarity is determined by the direction and momentum of the neutral particles.

C. Graphical Analysis of Inelastic Events

1. Ellipse Plots

In the following discussion, inelastic events

$$\pi^- + p \rightarrow \pi^- + p + \pi^0$$

and

$$\pi^- + p \rightarrow \pi^- + \pi^+ + n$$

are represented symbolically as

$$(M_1) + (M_4) \rightarrow (M_2) + (M_3) + (M_5).$$

Subscripts on kinematic variables indicate the particle to which the variable applies. Unstarred quantities and starred quantities pertain to the laboratory and center-of-mass (c.m.) systems respectively.

In the laboratory system that component of the momentum of the neutral particle, M_5, that is perpendicular to the plane defined by the two charged particles introduces a deviation from coplanarity and prevents the use of a geometrically simple dynamical representation in this reference frame. In the c.m. system the three final-state particles are coplanar, and, in this frame, ellipse plots may be used in the kinematic analysis. The ellipse plots for analysis of the two inelastic reactions are shown in Fig. 11.

The properties of each ellipse are established by the Lorentz transformation from the barsy system, (primed quantities) in which the virtual mass of particles M_3 and M_5 is at rest, to the c.m. system (see Fig. 12).

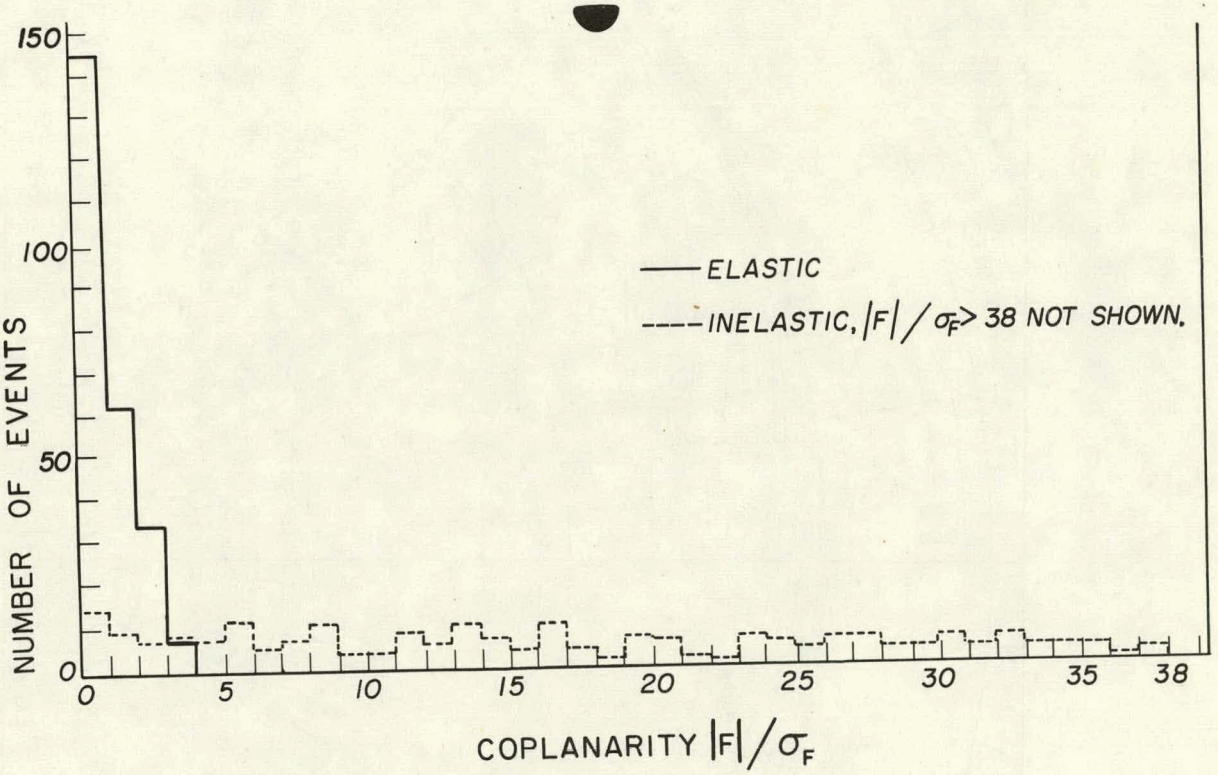

Fig. 10. Coplanarity of 250 elastic events (solid line) and 250 inelastic events (dotted line).

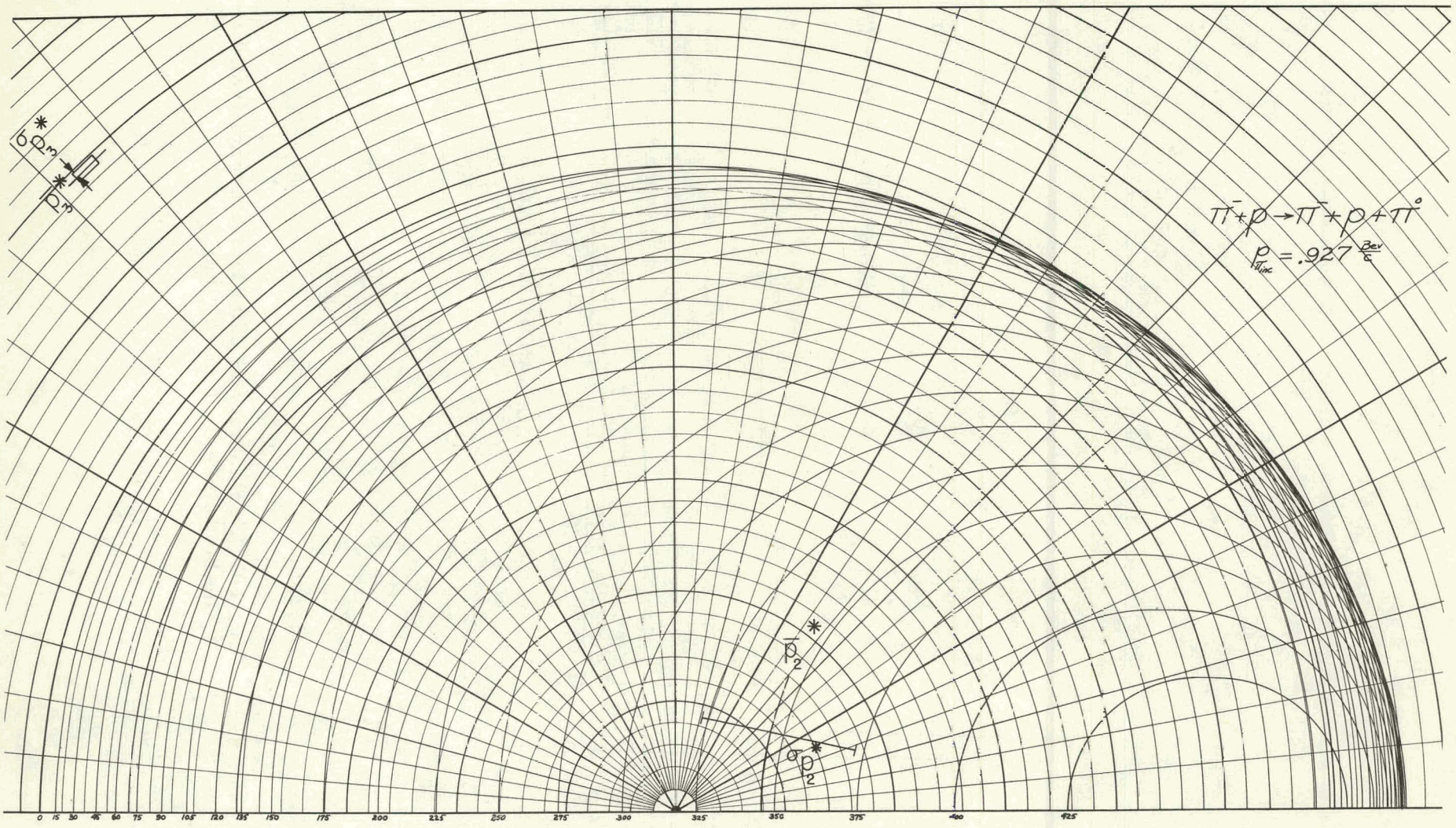

Fig. 11a. Ellipse plot for analysis of $\pi^- + p \rightarrow \pi^- + p + \pi^o$ inelastic events. A typical event is plotted.

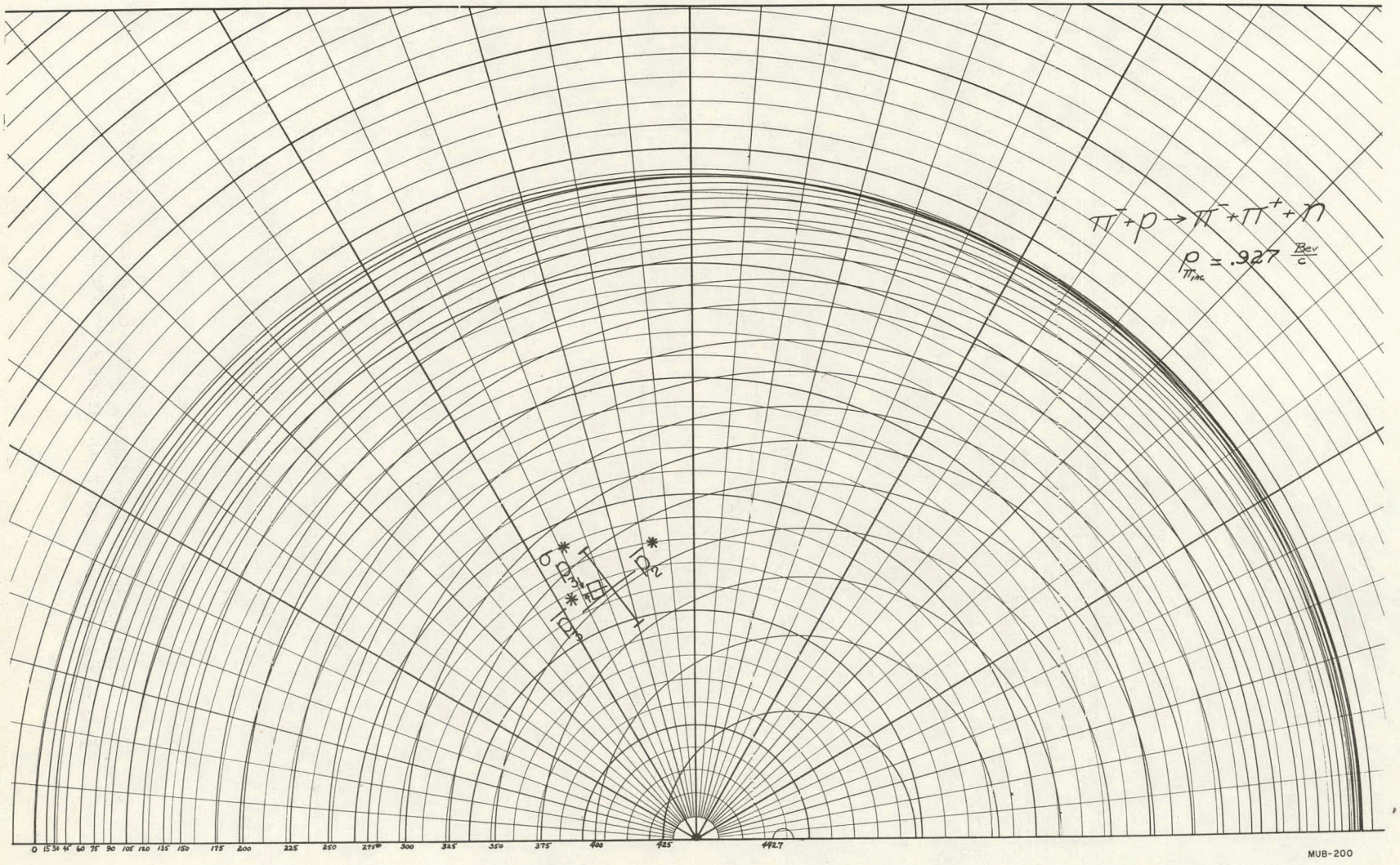

Fig. 11b. Ellipse plot for analysis of $\pi^- + p \rightarrow \pi^- + \pi^+ + n$ inelastic events. A typical event is plotted.

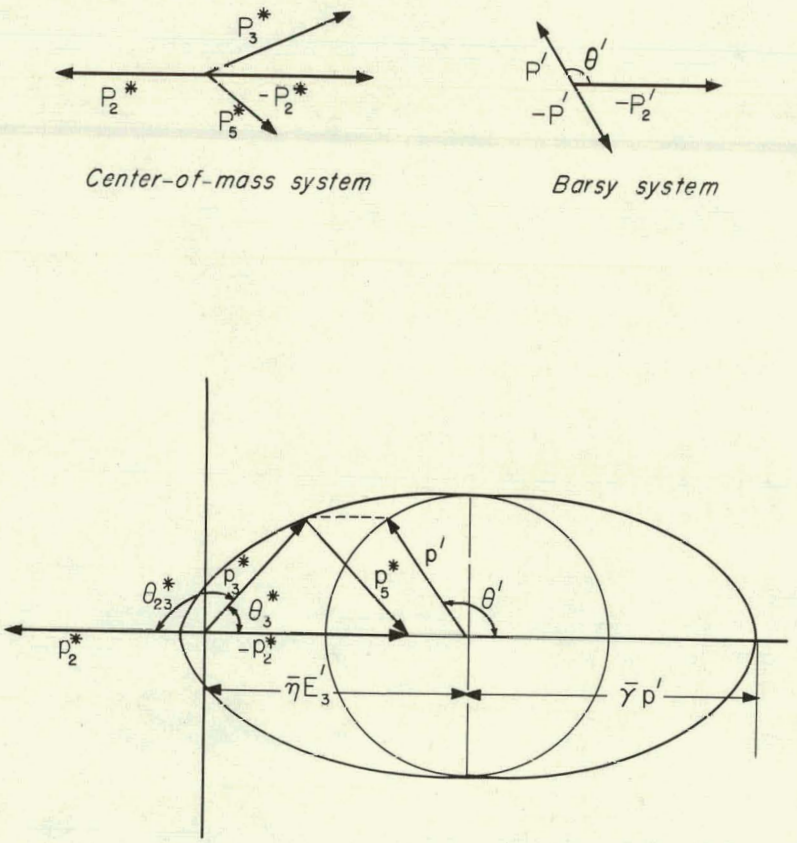

Fig. 12. Ellipse parameters, with diagram of transformation from barsy to center-of-mass system.

Thus for particle No. 3, ($p'_3 = -p'_5 = p'$; $\theta' = \theta'_3 = \pi - \theta'_5$), one can write

$$\begin{pmatrix} p^*_3 \cos\theta^*_3 \\ E^*_3 \end{pmatrix} = \begin{pmatrix} \bar{\gamma} & \bar{\eta} \\ \bar{\eta} & \bar{\gamma} \end{pmatrix} \begin{pmatrix} p'_3 \cos\theta'_3 \\ E'_3 \end{pmatrix} ,$$

only the longitudinal component of the momentum-energy vector being transformed. The quantities $\bar{\gamma}$ and $\bar{\eta}$ refer to the motion of the barsy relative to the c.m. system.

The origin of the ellipse is given by considering the special case in which the particle is going off at $\pi/2$ in the barsy,

$$p^*_3 \cos\theta^*_3 = \bar{\eta} E'_3 .$$

The major axis is the difference between the momentum vectors p^*_3 for the two special cases with $\theta' = 0$ and $\theta' = \pi$, i.e., $2\bar{\gamma} p'_3$. The minor axis is given simply by $2p'_3$.

Computation of the ellipse parameters necessary for construction of the ellipse plots was programmed for the IBM 650 by the following procedure.

(a) Calculate the virtual mass of particles No. 3 and No. 5,

$$m_{35} = [E^{*2} + M_2^2 - 2 E^* E^*_2]^{\frac{1}{2}} ,$$

where E^* is the total center-of-mass energy.

(b) Calculate $p^*_2(\max) = [(E^*_2(\max))^2 - M_2^2]^{\frac{1}{2}}$,

where

$$E^*_2(\max) = \frac{1}{2E^*} [E^{*2} + M_2^2 - (M_3 + M_5)^2] .$$

(c) Compute the ellipse parameters for increments of p^*_2 in the interval $0 \leq p^*_2 \leq p^*_2(\max)$, using the following expressions:

$$p' = \frac{1}{2m_{35}} [(m_{35} + M_3 + M_5)(m_{35} - M_3 - M_5)(m_{35} + M_3 - M_5)(m_{35} - M_3 + M_5)]^{\frac{1}{2}}, \quad \text{(Bev/c)}$$

$$\bar{\eta} E'_3 = 0.5 p^*_2 [1 + (M_3^2 - M_5^2)/m_{35}^2], \quad \text{Bev/c}$$

where

$$\bar{\gamma} = (E^* - E^*_2)/m_{35}; \quad \bar{\eta} = p^*_2 / m_{35} .$$

In both inelastic cases considered, the negatively charged particle is a π^-, and the positive particle in the final state characterizes the event.

2. Transformation to Center-of-Mass System

a. Rotation of Chamber Coördinate System

For the graphical analysis, a transformation of the measured momenta and angles of the prongs into the c.m. system is required. Propagation of the errors associated with these measured quantities into the new reference frame is also necessary.

Error propagation into the c.m. system was simplified by first rotating the measurement coördinate frame so as to bring the incident beam direction into coincidence with a transformation axis. In the coördinate system of the chamber, System I, Fig. 13, the direction vector of an incident π^- is nearly parallel to the positive y axis. System I was rotated to bring the beam direction into coincidence with the positive x' axis of System II.

The beam track in System I has polar and dip angles (ϕ_1, λ_1) defined, in terms of direction cosines, by

$$\sin\lambda_1 = n_{1z} \; ; \; \cos\lambda_1 = + \left[1 - n_{1z}^2\right]^{\frac{1}{2}} ;$$

$$\cos\phi_1 = n_{1x}/\cos\lambda_1 ; \; \sin\phi_1 = n_{1y}/\sin\lambda_1 .$$

It can be shown that rigid rotation of the coördinate System I through an angle of ϕ_1 about the x axis, followed by a rotation through an angle of $-\lambda_1$ about the new y axis brings about the desired alignment of the incident track and the $+x'$ axis of System II. Thus, a prong $\hat{n}$ represented in System I by

$$\hat{n} = \cos\lambda\cos\phi\,\hat{i} + \cos\lambda\sin\phi\,\hat{j} + \sin\lambda\,\hat{k}$$

will, in System II, have the form

$$\hat{n} = \sin\alpha\cos\beta\,\hat{i}' + \sin\alpha\sin\beta\,\hat{j}' + \cos\alpha\,\hat{k}',$$

with

$$\begin{pmatrix} \sin\alpha\cos\beta \\ \sin\alpha\sin\beta \\ \cos\alpha \end{pmatrix} = M(\phi_1, \lambda_1) \begin{pmatrix} \cos\lambda\cos\phi \\ \cos\lambda\sin\phi \\ \sin\lambda \end{pmatrix}.$$

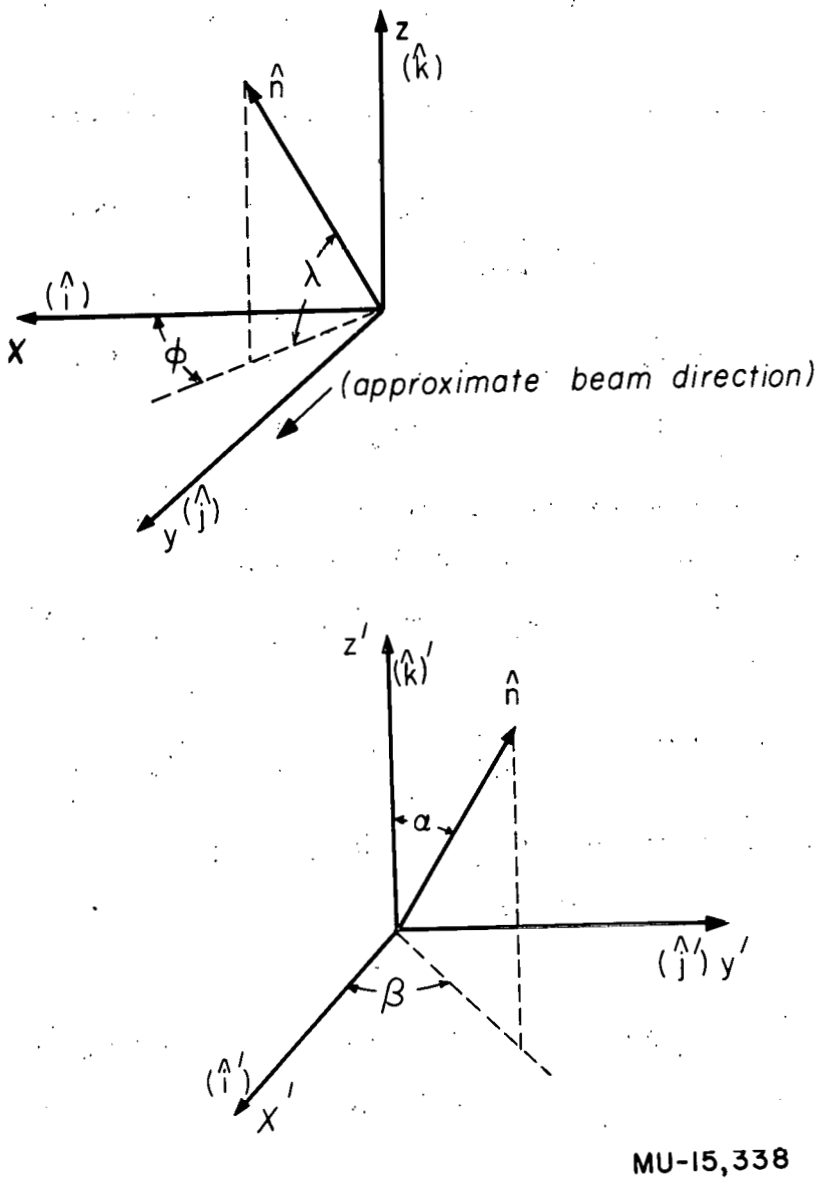

Fig. 13. Diagram of space coördinate systems used in error propagation to center-of-mass system. (Above) Chamber coördinates, System I. (Below) Transformation coördinates, System II.

The real orthogonal matrix $M(\phi_1, \lambda_1)$ is given by

$$M(\phi_1, \lambda_1) = \begin{pmatrix} \cos\lambda_1 \cos\phi_1 & \cos\lambda_1 \sin\phi_1 & \sin\lambda_1 \\ -\sin\phi_1 & \cos\phi_1 & 0 \\ -\sin\lambda_1 \cos\phi_1 & -\sin\lambda_1 \sin\phi_1 & \cos\lambda_1 \end{pmatrix}.$$

In System II the direction of the kth emergent prong is specified by

$$\cos\alpha_k = \cos\lambda_1 \sin\lambda_k - \sin\lambda_1 \cos\lambda_k \cos(\phi_k - \phi_1),$$

$$\sin\alpha_k = +\sqrt{1 - \cos^2\alpha_k},$$

$$\cos\beta_k = \frac{1}{\sin\alpha_k}\left[\cos\lambda_1 \cos\lambda_k \cos(\phi_k - \phi_1) + \sin\lambda_1 \sin\lambda_k\right],$$

$$\sin\beta_k = \frac{1}{\sin\alpha_k}\left[\cos\lambda_k \sin(\phi_k - \phi_1)\right].$$

It can be shown that the errors in α and β associated with errors in ϕ and λ are, for the kth prong,

$$\sigma_{\alpha_k}^2 = A_{1k}^2\left[(\sigma_{\phi_1})^2 + (\sigma_{\phi_k})^2\right] + A_{2k}^2(\sigma_{\lambda_1})^2 + A_{3k}^2(\sigma_{\lambda_k})^2,$$

$$\sigma_{\beta_k}^2 = B_{1k}^2\left[(\sigma_{\phi_1})^2 + (\sigma_{\phi_k})^2\right] + B_{2k}^2(\sigma_{\lambda_1})^2 + B_{3k}^2(\sigma_{\lambda_k})^2,$$

where the coefficients $A_{1k}, \cdots, B_{3k}$ are given by

$$A_{1k} = \sin\beta_k \sin\lambda_1,$$

$$A_{2k} = \cos\beta_k,$$

$$A_{3k} = \cos\lambda_1 \cos\lambda_k + \sin\lambda_1 \sin\lambda_k \cos(\phi_k - \phi_1),$$

$$B_{1k} = \frac{1}{\sin^2\alpha_k} \cos\lambda_k A_{3k},$$

$$B_{2k} = \frac{1}{\sin\alpha_k} \cos\alpha_k \sin\beta_k,$$

$$B_{3k} = \frac{\sin\lambda_1 \sin\beta_k}{\sin\alpha_k \cos\lambda_k}.$$

b. Center-of-Mass System Quantities

Following the axis rotation the incident-particle track coincides with the + x' axis of System II, and this axis is the transformation axis and the reference axis for angle measurements; θ_k is the laboratory space angle for the kth prong.

For the kth prong, we can write

$$\begin{pmatrix} p_k^* \cos\theta_k^* \\ E_k^* \end{pmatrix} = \begin{pmatrix} \bar{\gamma} & -\bar{\eta} \\ -\bar{\eta} & \bar{\gamma} \end{pmatrix} \begin{pmatrix} p_k \cos\theta_k \\ E_k \end{pmatrix} ,$$

and the center-of-mass momenta necessary for graphical analysis are given by

$$p_k^* = p_k \left[\sin^2\theta_k + \bar{\gamma}^2\left(\cos\theta_k - \frac{\bar{\beta}}{\beta_k}\right)^2\right]^{\frac{1}{2}}, \qquad (k = 2, 3) \qquad (V\text{-}1)$$

where

$$\beta_k = \frac{p_k}{\sqrt{p_k^2 + M_k^2}} , \quad \cos\theta_k = \sin\alpha_k \cos\beta_k, \quad \sin^2\theta_k = 1 - \cos^2\theta_k .$$

The angular separation of the two emergent prongs in the c.m. system, $\theta_{2,3}^*$, can be calculated from the invariance of $\mathcal{M}_{2,3}^2$, i.e.,

$$\mathcal{M}_{2,3} = M_2^2 + M_3^2 + 2E_2E_3 - 2p_2p_3\cos\theta_{23}$$

$$= M_2^2 + M_3^2 + 2E_2^*E_3^* - 2p_2^*p_3^*\cos\theta_{23}^* ;$$

hence

$$\theta_{23}^* = \cos^{-1}\left(\frac{E_2^*E_3^* - E_2E_3 + p_2p_3\cos\theta_{23}}{p_2^*p_3^*}\right) , \qquad (V\text{-}2)$$

with $\cos\theta_{23} = \sin\alpha_2 \sin\alpha_3 \cos(\beta_2 - \beta_3) + \cos\alpha_2 \cos\alpha_3$

and

$$E_k^* = \sqrt{p_k^{*2} + M_k^2} .$$

From Eq. (V-1) it can be shown that the standard deviation of the error associated with the kth prong's momentum (c.m.) is

$$\sigma_{p_k^*} = \frac{p_k}{p_k^*} \left[(C_k \sigma_{p_k})^2 + (D_k \sigma_{\theta_k})^2 \right]^{\frac{1}{2}},$$

where

$$C_k = \left(\frac{p_k^*}{p_k} \right)^2 + \frac{\bar{\eta} M_k^2}{\bar{E}_k p_k} \bar{\gamma} \left(\cos\theta_k - \frac{\bar{\beta}}{\beta_k} \right),$$

$$D_k = p_k \left[\sin\theta_k \cos\theta_k (1 - \bar{\gamma}^2) + \frac{\bar{\gamma} \bar{\eta}}{\beta_k} \sin\theta_k \right],$$

and

$$\sigma_{\theta_k} = \left| \frac{1}{\sin\theta_k} \right| \left[(\sin\alpha_k \sin\beta_k)^2 \sigma_{\beta_k}^2 + (\cos\alpha_k \cos\beta_k)^2 \sigma_{\alpha_k}^2 \right]^{\frac{1}{2}}.$$

The error in θ_{23}^*, a function of the six variables (p_2, p_3, α_2, β_2, α_3, β_3) that define tracks No. 2 and No. 3, was obtained by evaluating the required partial derivatives of Eq. (V-2) as difference quotients rather than programming in their analytical expressions.

The center-of-mass quantities are, of course, dependent on the reaction assumed, i.e., the mass assigned to particle No. 3. The computer program first computes the quantities using $M_3 = M_p$; then the calculation is repeated with $M_3 = M_\pi$.

For each event the two inelastic reactions are considered in turn; and the areas, defined by p_3^*, $\cos\theta_{23}^*$, and their associated errors, are plotted on the appropriate set of curves. For one of the two reactions the terminal point of p_3^* will, ideally, lie (within errors) on the ellipse specified by the value of p_2^*, thereby characterizing the reaction. A typical event has been plotted in Fig. 11. The values of p_2^*, p_3^*, and the standard deviation $\sigma_{p_2^*}$, $\sigma_{p_3^*}$ are used in determining the best graphical fit. The quantity to be minimized in each instance is

$$\chi^2 = \left(\frac{x - x_3}{\sigma_3} \right)^2 + \left(\frac{x - x_2}{\sigma_2} \right)^2,$$

where $x_i = p_i^*$, $\sigma_i = \sigma_{p_i^*}$ $(i = 2, 3)$.

One can write

$$\chi^2_{(\min)} = \frac{(x_2 - x_3)^2}{\sigma_2^2 + \sigma_3^2} .$$

The values of $\chi^2_{(\min)}$ for the inelastic interpretations were compared for determination of the correct graphical interpretation. For the event plotted in Fig. 11, the missing neutral is obviously a neutron; $\chi^2_{\pi 0}/\chi^2_n = 99$. A detailed discussion of the graphical separation of inelastic events is not given. In summary, separation by this method was identical to the separation obtained by the computer program discussed in the following section.

D. Computer Program for Kinematic Analysis of Two-Prong Events

1. General

Kinematic analysis of two-prong events--i.e., events having one incident π^- track and two charged outgoing tracks--was programmed for the IBM-650. The input data consist of the measured values of nine dynamical variables x_i (specified below) characterizing each event, and for each measured variable its associated standard deviation, σ_i. Output data consist of (a) the least-squares adjusted value of each of the nine variables required to make a "best fit" to each of three possible interpretations, (e.g., elastic, and inelastic with missing π^0 or neutron); (b) the value of χ^2 and a number of allied statistical consistency tests; (c) the momentum and trajectory of the missing neutral particle (π^0 or neutron).

2. Choice of Dynamical Variables

The nine dynamical variables $x_i (i = 1, 2, \cdots, 9)$ consist of three curvature variables ($j = 1, 2, 3$),

$$K_j = \frac{\pm 1}{|p_j| \cos \lambda_j} , \qquad (\text{Bev/c})^{-1}$$

where

$$\pm = \begin{cases} +1 \text{ for incident track, track No. 1} \\ -1 \text{ for outgoing prongs, tracks Nos. 2 and 3} \end{cases} ;$$

the three dip tangents

$$\tan\lambda_j, \qquad (j = 1, 2, 3);$$

and the three azimuthal angles

$$\phi_j \qquad (j = 1, 2, 3).$$

These variables were chosen because of correspondence with quantities most directly measured from the stereo projections on a scanning table. Curvature was chosen in preference to the more familiar momentum variable to eliminate the following problem: the use of momentum as one of the fitting variables introduces an artificial mathematical discontinuity at high particle momentum. For example, two beam tracks of momentum 4.0 Bev/c and opposite charge are indistinguishable by present techniques. Their momenta, however, are two large numbers of opposite sign, whereas their curvatures are essentially zero in both cases. At lower momenta this difficulty again shows up as a skewness in momentum error.

3. Interpretation Defined

The general two-prong interaction may be written symbolically as

$$(M_1) + (M_4) \rightarrow (M_2) + (M_3) + (M_5),$$

where

M_1 = incident particle (track No. 1)

M_4 = struck particle,

M_2 = track No. 2 particle,

M_3 = track No. 3 particle,

M_5 = missing neutral (not used if elastic).

An interpretation consists, by definition, of two statements:

1. Whether the event is to be treated as elastic or inelastic;

2. The set of masses M_1, M_2, M_3, M_4 -- and, for inelastic interpretations, M_5.

4. Kinematic Equations of Constraint

For any given interpretation the momentum and energy $(-)F_\lambda$ ($\lambda = 1, 2, 3, 4$) of the missing neutral, if any, can be written as

$$F_1 = (-) \sum_{j=1}^{3} \cos\phi_j / K_j, \tag{V-3}$$

$$F_2 = (-) \sum_{j=1}^{3} \sin\phi_j / K_j, \tag{V-4}$$

$$F_3 = (-) \sum_{j=1}^{3} \tan\lambda_j / K_j, \tag{V-5}$$

$$F_4 = (-) (M_4 + E_1 - E_2 - E_3), \tag{V-6}$$

where the energy of the jth particle is computed from

$$E_j = \left[\frac{(1 + \tan^2\lambda_j)}{K_j^2} + M_j^2 \right]^{\frac{1}{2}},$$

with M_j the mass of the jth particle. Here M_4(Bev) is the mass of the struck particle.

The kinematic constraints can be summarized into two groups according to whether the event is treated as elastic or inelastic:

1. Elastic: Impose four contraints, $F_\lambda(x) = 0$ for $\lambda = 1, 2, 3, 4$.
2. Inelastic: Impose the single constraint, $\zeta(x) = 0$,

where ζ is defined by the expression

$$\zeta = \begin{cases} M_5 - |Q|^{\frac{1}{2}} & Q \geq 0 \\ M_5 + |Q|^{\frac{1}{2}} & Q < 0 \end{cases}$$

where

$$Q = (-) F_\lambda \tilde{F}_\lambda = F_4^2 - \sum_{i=1}^{3} F_i^2 .$$

For Q positive, $|Q|^{\frac{1}{2}}$ is the apparent mass of the missing neutral.

The quadratic dependence of ζ on F_4 makes it possible to reach a least-squares fit for which the energy of the missing neutral is negative, i.e., $F_4 > 0$. These erroneous solutions are fortunately infrequent and easily detected.

The particular kinematic constraints selected above are somewhat arbitrary. For example, one of the elastic constraints could have imposed the coplanarity restriction. Almost any function $G(M_5^2-Q)$ such that $G(0)$ was zero could have been used for the inelastic constraint. The kinematic constraints cited above were selected first for their ease of computation, and second for their essentially linear dependence on the dynamical variables in the range of physical interest.

5. Definition of a Kinematic Fit

In general the measured values x_i^M of the nine variables of an event do not satisfy the kinematic constraints. Therefore a least-squares adjustment of this input data is required with the measured quantities, x_i^M, going to the adjusted values, x_i: $x_i^M \rightarrow x_i$ $(i = 1, 2 \cdots 9)$.

A least-squares fit to a given interpretation is specified by a set of dynamical variables x_i satisfying two conditions:

(a) The constraints are individually equal to zero, i.e., $F_\lambda(x_i) = 0$, for all constraints $\lambda = 1, \cdots c$. For inelastics F_1 is set equal to ζ and $c = 1$.

(b) The chi-square quantity,

$$\chi^2(x_i) = \sum_{i=1}^{9} \left(\frac{x_i - x_i^M}{\sigma_i} \right)^2,$$

is at a minimum (or stationary) point for all variations, δx_i, about x_i consistent with the kinematic constraints.

An alternative, but equivalent, formulation using Lagrangian multipliers proves more mathematically tractable. This choice replaces (a) and (b) by this requirement:

The modified chi-square quantity

$$M(x_i, a_\lambda) = \chi^2 + 2 \sum_{\lambda=1}^{c} a_\lambda F_\lambda(x_i) \qquad (V-7)$$

is minimum (or stationary) under arbitrary variations, δa_λ, δx_i of all variables about their stationary values, a_λ, x_i.

6. Statistical Estimates of the Quality of the Fit

Achievement of a "fit" is a purely mathematical achievement in programming; in no way does it assure that the selected interpretation is valid. Therefore, a statistical estimate of the quality of the fit to a given interpretation is required.

The adjustment parameters are normalized by introducing the quantities ξ_i,

$$\xi_i = (x_i - x_i^M) / \sigma_i \qquad (i = 1, \cdots, 9).$$

The foremost quantity for the statistical estimate is, of course,

$$\chi^2 = \sum_{i=1}^{9} \xi_i^2$$

evaluated at the "fit." If χ^2 is in the doubtful zone, being neither unduly large nor sufficiently small, other tests can be quite useful.

In particular a distinction is made between: (a) "errors" from inherent inaccuracy of measurement and from turbulence, as discussed in Section IV; and (b) "bloopers" caused by miscoding, measurement of wrong fiducials, or jumping to a neighboring track, or digitizer errors. In addition, it is helpful to distinguish three statistical estimates that were used.

(i) Global: the tests $|\xi_i| < 3$. These tests are dependent only upon x_i at fit, the measured x_i^M, and the standard deviation in the variable, σ_i.

(ii) Local: the tests $|\xi_i / \sigma_{\xi_i}| < 3$. These tests are peculiar to the interpretation fitted. Here σ_{ξ_i} is the standard deviation in ξ_i itself. Such tests exploit the derivatives of the constraints at fit and are often more sensitive than the global test, provided the interpretation is correct.

(iii) Systematic: correlation of curvature and azimuthal angle errors, incorrect nominal beam momentum, and neglect of dE/dx corrections in curvature measurement. Corrections of this nature were made by hand calculation where required for resolution of otherwise ambiguous interpretations.

7. Trajectory of the Missing Neutral Particle

The variables appropriate to the missing neutral track--i.e., curvature, K_5; dip tangent, $\tan\lambda_5$; and azimuthal angle, ϕ_5--are calculated for each inelastic interpretation. When a fit has been obtained, these quantities are specified by

$$K_5 = (p_5 \cos\lambda_5)^{-1} = (F_1^2 + F_2^2)^{-\frac{1}{2}}, \qquad (\text{Bev/c})^{-1}, \quad \text{(V-8)}$$

$$\tan\lambda_5 = F_3/(F_1^2 + F_2^2)^{\frac{1}{2}} = F_3 K_5, \quad \text{(V-9)}$$

$$\phi_5 = \arctan(F_2/F_1), \quad \text{(V-10)}$$

where $-F_1$, $-F_2$, $-F_3$ is the momentum vector of the missing neutral, Eqs. (V-3), (V-4), and (V-5).

8. Mathematics of the Fitting Procedure

a. Linear Constraints

The procedure introduced here was developed by Frank T. Solmitz and Horace Taft.[16,17] Let us examine the fitting problem for the special case, in which the constraints constitute linear relations between the x_i,

$$F_\lambda(x_i) = g_\lambda + \sum_{i=1}^{9} F_{\lambda i} x_i, \quad \text{(V-11)}$$

where $F_{\lambda i} = \partial F_\lambda / \partial x_i$. We now require the (9+c) partial derivatives of M, Eq. (V-7) to be zero:

$$\frac{\partial M}{\partial x_i} = 0: \quad \xi_i = -\sum_\lambda a_\lambda F_{\lambda i} \sigma_i; \quad \text{(V-12)}$$

$$\frac{\partial M}{\partial a_i} = 0: \quad F_\lambda(x_i) = 0. \quad \text{(V-13)}$$

Substituting Eq. (V-12) into (V-13), we get c equations for the a_λ's:

$$\sum_\lambda a_\lambda H_{\lambda\mu} = F_\lambda(x^M), \quad \text{(V-14)}$$

where $H_{\lambda\mu}$ is the symmetric matrix,

$$H_{\lambda\mu} = \sum_{i=1}^{9} (F_{\lambda i}\sigma_i)(F_{\mu i}\sigma_i). \quad \text{(V-15)}$$

Hence we have

$$a_\lambda = \sum_\mu H_{\lambda\mu}^{-1} \; F_\mu, \tag{V-16}$$

which, when substituted back into Eq. (V-12), gives the adjusted values of x_i.

b. Nonlinear Constraints

Solmitz has suggested the adaptation of this method to the solution of the fitting problem for nonlinear constraints.[16] For a point x_i^ν in the neighborhood of the fitted values x_i the nonlinear constraints can be approximated by the linear expansion

$$F_\lambda(x_i) = F_\lambda(x_i^\nu) + \partial F/\partial x_i \,|_{x_i^\nu} (x_i - x_i^\nu). \tag{V-17}$$

The method of successive approximation, using equations paralleling Section VD8(a) is then used to derive better estimates, x_i^ν, of the fit variables x_i.

The fundamental Eqs. (V-12) and (V-13) carry over directly; the quantities $F_{\lambda i}$ must be here reinterpreted as partial derivatives:

$$F_{\lambda i} = \frac{\partial}{\partial x_i} F_\lambda \; . \tag{V-18}$$

Given the νth approximation (x_i^ν, a_λ^ν) to the solution of the fundamental Eq. (V-12) and (V-13), one deduces the next iteration $(\nu+1)$ from a first-order expansion in $(x_i - x_i^\nu)$:

$$\xi_i^{\nu+1} = - \sum_\lambda a_\lambda^{\nu+1} \; F_{\lambda i}^\nu \; \sigma_i, \tag{V-19}$$

$$F_\lambda^\nu + \sum_{i=1}^{9} (\xi_i^{\nu+1} - \xi_i^\nu) F_{\lambda i}^\nu \; \sigma_i = 0. \tag{V-20}$$

Introducing the two quantities $H_{\lambda\mu}^\nu$, $a_\lambda^{\nu+1}$ generalizing Expressions (V-15) and (V-16), and the modified constraint function f_λ^ν, one has

$$H_{\lambda\mu}^\nu = \sum_i (F_{\lambda i}^\nu \; \sigma_i)(F_{\mu i}^\nu \; \sigma_i), \tag{V-21}$$

$$a_\lambda^{\nu+1} = \sum_\mu (H^\nu)_{\lambda\mu}^{-1} \; f_\mu^\nu, \tag{V-22}$$

$$f_\lambda^{\nu} = F_\lambda^{\nu} + \sum_i \xi_i^{\nu} F_{\lambda i}^{\nu} \sigma_i \; ; \qquad \text{(V-23)}$$

$\xi_i^{\nu+1}$ is obtainable by substitution of $a_\lambda^{\nu+1}$ into Eq. (V-19).

This iteration process can be initiated with "zeroth-approximation" values $x_i^{(0)} = x_i^M$, i.e., $\xi_i^{(0)} = 0$.

9. Statistical Correlation of Adjusted and Measured Variables

The measured variables x_i^M are assumed to be uncorrelated:

$$\overline{\delta x_i^M \, \delta x_j^M} = \delta_{ij} \sigma_i^2, \qquad \text{where } \sigma_i$$

is the standard deviation in the measurement of x_i^M. However, the fitted variables x_i are correlated as a result of the fitting process. The normalized displacements $\xi_i (i = 1, \cdots 9)$ are also correlated.

Evaluation of the fit achieved for any interpretation is possible only if we establish two references: (a) the standard deviation, σ_{ξ_i}, of ξ_i itself; and (b) the average value of χ^2 to be expected with c constraints, using the fitting procedure.

These results can be deduced as follows. At χ^2 minimum the normalized displacement ξ_i is given by

$$\xi_i = - \sum_{\mu, \nu} f_\mu \, H_{\mu\nu}^{-1} (F_{\nu i} \sigma_i),$$

and accordingly the variation $\delta \xi_i$ is

$$\delta \xi_i = - \sum_{\mu, \nu} \delta f_\mu \, H_{\mu\nu}^{-1} (F_{\nu i} \sigma_i).$$

Using the result of Solmitz,[16] valid only to the extent that the region near χ^2 minimum can be treated as linear,

$$\overline{\delta f_\mu \, \delta f_\nu} = H_{\mu\nu},$$

then one deduces

$$\sigma_{\xi_i}^2 = \overline{(\delta \xi_i)^2}$$

$$= \sum_{\mu, \nu=1}^{c} (F_{\mu i} \sigma_i) H_{\mu\nu}^{-1} (F_{\nu i} \sigma_i).$$

Not all standard deviations σ_{ξ_i} are equal to unity, because in a least-squares fitting those dynamical variables least well known are, in general, adjusted (shifted) by a greater number of standard deviations in the fitting process. The digital computer was programmed to evaluate and print out the adjustment variables ξ_i/σ_{ξ_i}, which have in principle a unit-width normal distribution.

The mean value of χ^2 can now be established as a special result:

$$\overline{\chi^2} = \overline{\sum_i \xi_i^2} = \sum_i \sigma_{\xi_i}^2$$

$$= \sum_{i,\mu,\nu=1}^{c} (F_{\mu i}\sigma_i)(F_{\nu i}\sigma_i) H_{\mu\nu}^{-1}$$

$$= c, \text{ the number of constraints.}$$

In summary, χ^2 should average to 1 and 4 for the inelastic and elastic events, respectively. The χ^2 distributions for the inelastic and elastic events are shown in Fig. 14.

10. Comparison of Measured and Computed Quantities

Figure 15 shows a photograph of a $\pi^- + p \rightarrow \pi^- + \pi^+ + n$ interaction. A schematic diagram of the event is shown in Fig. 16. This is a typical two-prong event if we consider only tracks Nos. 1, 2, and 3. (The kinematic program considers only these tracks.) In this event, the missing neutron (neutral track No. 4) strikes a proton, track No. 5, and the neutron momentum and trajectory can be calculated from the direction and range of this stopping proton. This fortuitous circumstance permits the following tests of the kinematic program. (a) Does the program, utilizing only measurements of tracks Nos. 1, 2, and 3, achieve a "fit" for the neutron interpretation? (b) Do the computed trajectory and momentum of the neutron agree with the measured values (based on the vertex, the first bubble of the proton track, and the range of the stopping proton)? Table III summarizes the comparison between measured and computed quantities. The large measurement error associated with the dip angle of the neutron

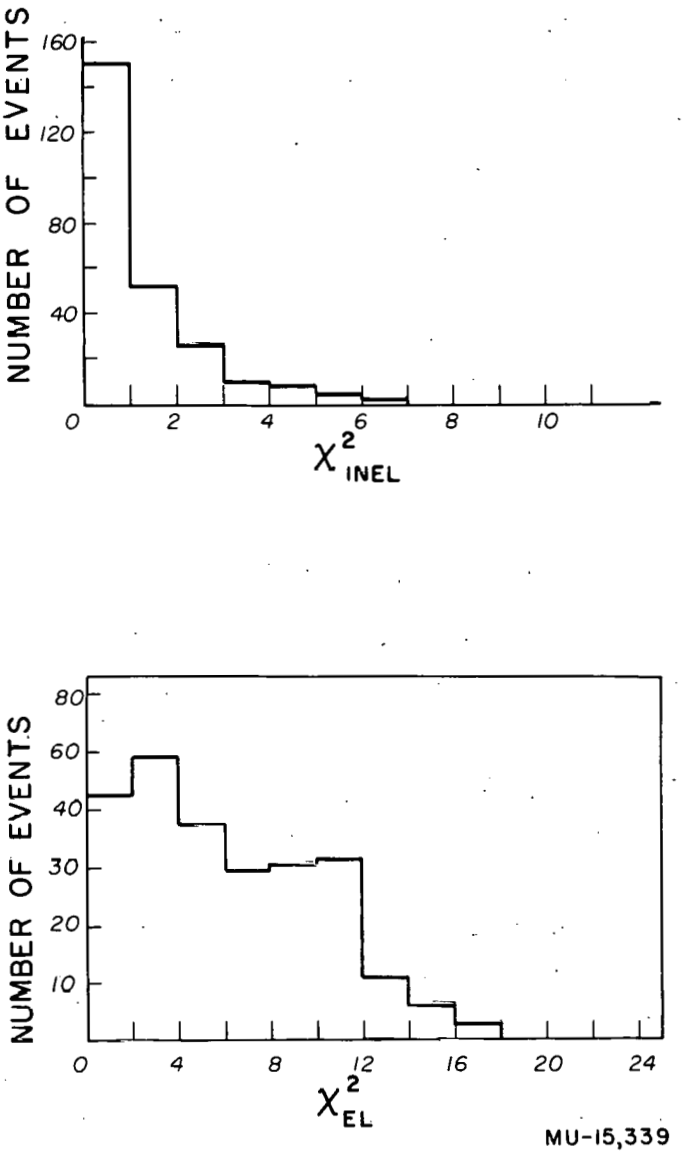

Fig. 14. (Above) χ^2 inelastic interpretation, 250 inelastic events
(Below) χ^2 elastic interpretation, 250 elastic events.

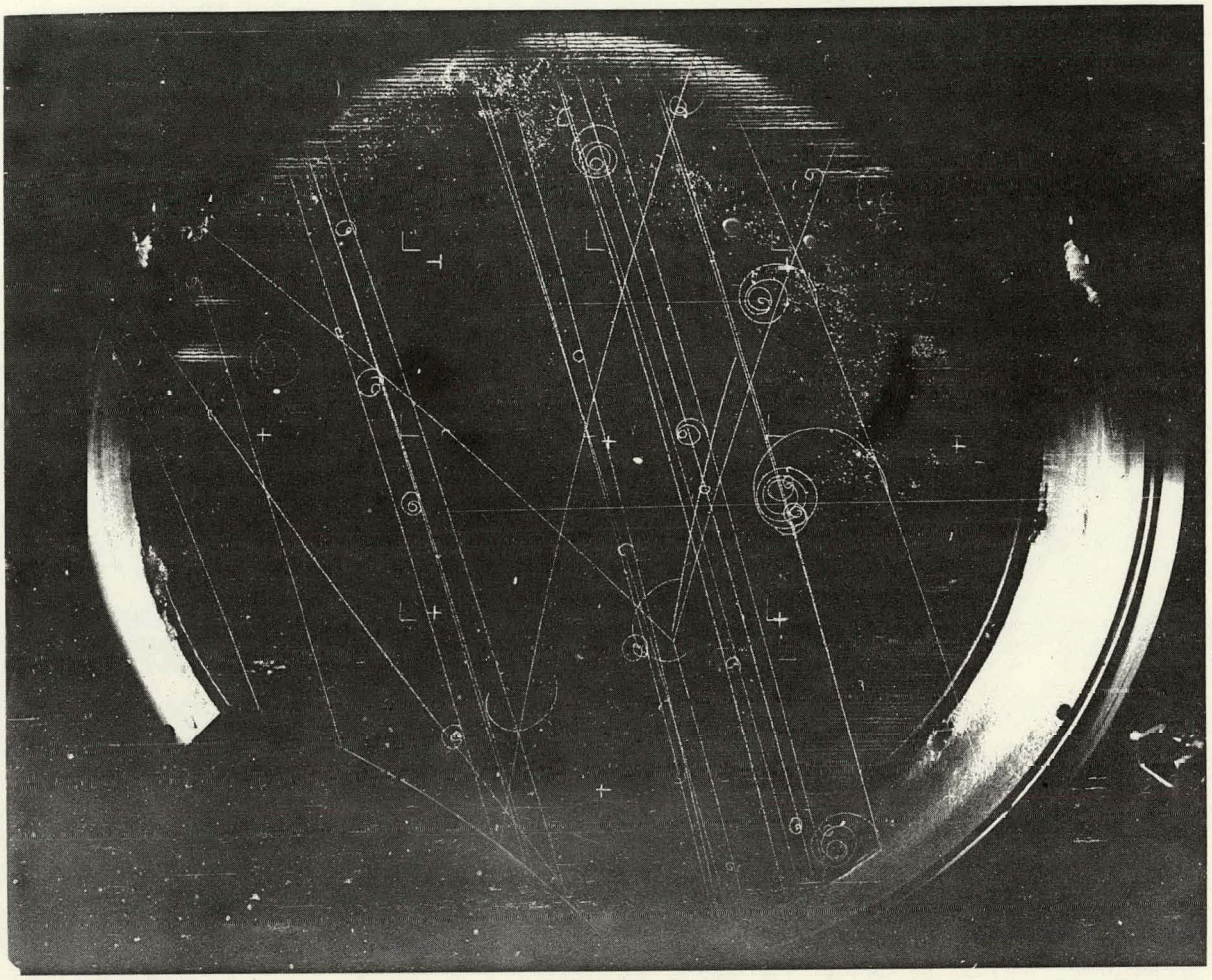

ZN-1941

Fig. 15. Photograph of $\pi^- + p \rightarrow \pi^- + \pi^+ + n$ event (neutron scattering) in the bubble chamber.

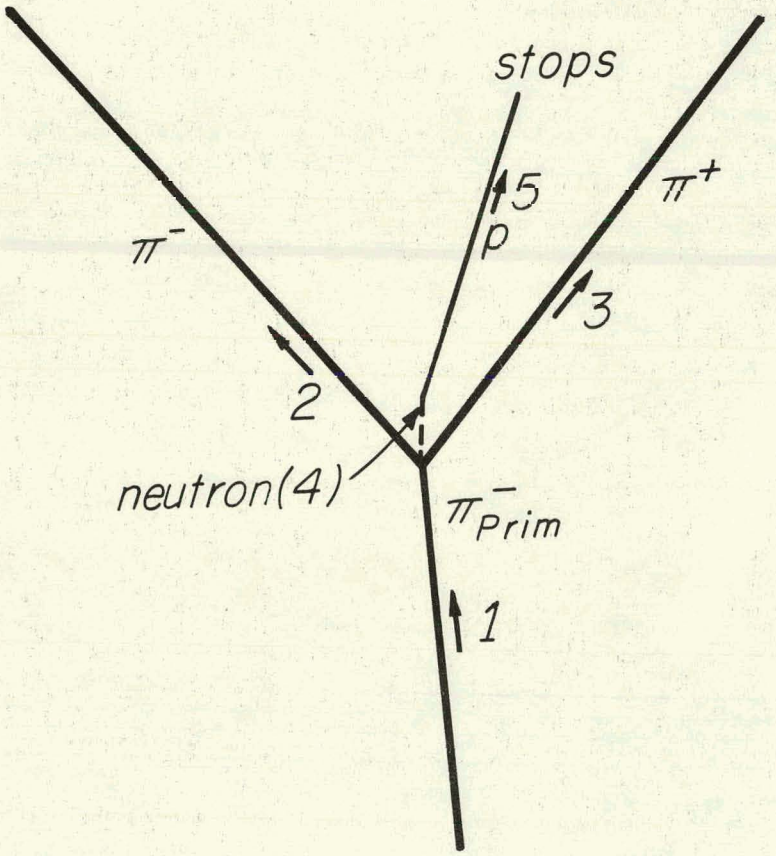

Fig. 16. Schematic diagram of $\pi^- + p \rightarrow \pi^- + \pi^+ + n$ event.

is caused by the shortness of the track and the fact that only two points were available for measurement. The measurement errors for the π^+ (a typical track) are included in Table III.

Table III

Measured and adjusted quantities

Particle	Quantity	Value from measurements	Measurement error	Least-squares value
proton, No. 5	range	7.178 cm	—	
	p_5	0.243 Bev/c	0.002 Bev/c	
neutron, No. 4	p_4	0.256 Bev/c	0.036 Bev/c	0.267 Bev/c
	ϕ_4	95.1°	4.2°	93.1°
	λ_4	19.3°	38.0°	25.4°
	length (meas.)	0.325 cm	—	—
—	χ^2_{el}			>99.9
	χ^2_n			2.0
π^+ No. 3	p_3	0.388 Bev/c	0.025 Bev/c	0.372 Bev/c
	ϕ_3	74.7°	0.2°	74.7°
	λ_3	11.9°	0.5°	12.0°
	length (meas.)	13.138 cm.	—	—

VI. CLASSIFICATION OF EVENTS

All events were first examined for the value of the coplanarity function F/σ_F, and catalogued as coplanar ($F/\sigma_F < 4$) or non-coplanar ($F/\sigma_F \geq 4$).

The noncoplanar events were considered to be definitely inelastic, and were subdivided as follows:

(A.1) Strongly separable by χ^2, i.e., $\chi^2_{\pi^0} \leq 2.7$, $\chi^2_n \geq 5$, or vice versa. Final classification of these events corresponds to the smaller χ^2.

(A.2) Tentatively ambiguous, i.e., both $\chi^2_{\pi^0}$ and $\chi^2_n \leq 5$. These events were examined for delta rays and ionization of the positive track, and kinematically examined on the p_0, p_+ plot described below.

(A.3) All others - not having satisfactory χ^2 for either the π^0 or neutron interpretation. These events were examined on the scanning desk for measurement and (or) coding errors, remeasured or adjusted by template fittings, and finally forced into category A.1 or A.2.

The coplanar events, $|F/\sigma_F| < 4$, were divided into classes in an analogous way:

(B.1) Strongly separable as elastic, by χ^2

(B.2) Elastic or π^0 (ambiguous); neither ionization nor delta rays can possibly resolve the ambiguity.

(B.3) Elastic or neutron (ambiguous); possible to resolve by identification of positive track, on the basis of ionization and delta rays.

(B.4) Neutron or π^0 (ambiguous); separable as class A.2.

(B.5) No fit achieved; events remeasured.

All the events with $|F/\sigma_F| < 4$ and fitting only inelastic interpretations were re-examined for gross measurement errors. These errors can induce a spurious π^0 or neutron fit.

Positive-particle identification, based on ionization, was used in the classification of otherwise ambiguous events. The incident π^- was used as the local minimum-ionization standard. (Calibration of the chamber for bubble density as a function of ionization was not feasible

for two reasons: (a) chamber sensitivity was kept high to detect neutral-particle end points; (b) superposition of bubbles--especially for steeply dipping tracks--makes bubble counting unreliable.) Low-momentum protons were readily identified in the chamber.

It is quite possible for an inelastic event to be kinematically ambiguous, even in the limit of exact momentum and angle measurements. To see this let p_+ be the observed momentum of the positive prong, and let p_0 be the calculated momentum of the missing neutral (π^0 or neutron). Normally the energy available to the positive and neutral particles, as calculated from the conservation of energy and the known masses of the incident and struck particles, allows assignment of only one mass to the positive particle and one mass to the neutral particle (either proton mass and π^0 mass, or π^+ mass and neutron mass). However, to the approximation that the small $\pi^0 - \pi^+$, n - p mass differences can be neglected, kinematic separation fails for $p_0 = p_+$. Although such events are kinematically ambiguous, they may, of course, be classified on the basis of delta rays or ionization along the positive track.

Figure 17 shows the p_0, p_+ distribution of a group of 26 events of class A-2. The ambiguous $p_0 = p_+$ line is broadened by the typical measurement error of p_+; the error increases with increasing positive momentum. For the most part, those events with good χ^2 separation have the better interpretation (π^0 or n) outside the ambiguity region.

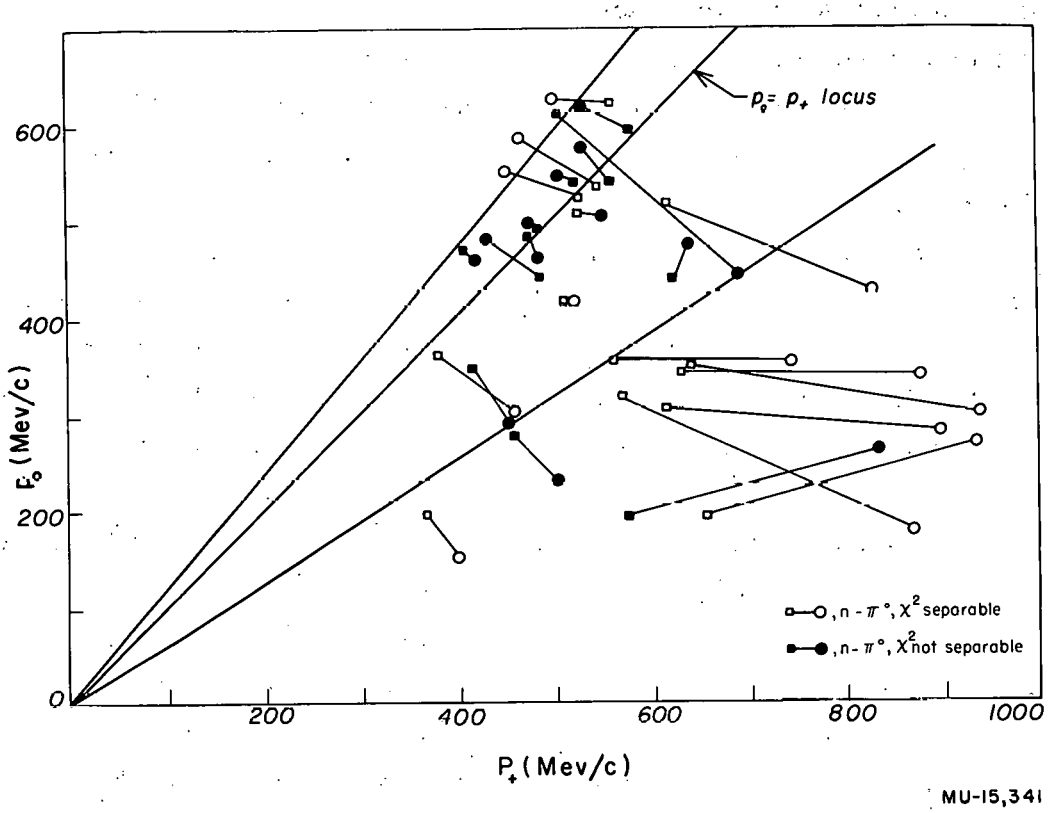

Fig. 17. Scatter diagram of positive and neutral particle momenta (26 events). Kinematically ambiguous region delineated.

VII. RESULTS

A. Cross Sections

The total number of interactions, corrected for over-all scanning efficiency and detection dependence upon the orientation of the plane of emergent prongs is 1430 ± 43. After correcting for the small-angle elastic scattering, the total number of events occurring in the acceptance volume of the chamber is increased to 1452 ± 48.

The total number of interactions and the integrated pion path length in the acceptance volume provides a direct measurement of the total cross section. Beam tracks crossing the acceptance volume, as projected in one view, were counted in every tenth frame of film. Based on this beam count and the average track length across the acceptance volume, a total pion path length of 7.76×10^5 cm ± 1.1% was computed. This length includes corrections for muon contamination (1.0 ± 1.0%) and electron contamination (1.8 ± 1.2%).[18] The π^--p total cross section found is 53.3 ± 2.4 millibarns. The cross sections for all zero-, two-, four-, and six-prong and V-particle events observed are listed in Table IV, together with their relative frequencies.

Table V gives the relative frequencies and cross sections for the elastic-scattering and single-pion-production reactions.

B. Elastic Differential Cross Section

Figure 18 shows the elastic π^--p differential cross section. This differential cross section displays the narrow diffraction peak in the forward direction, and after dropping to a distinct mimimum from 66° to 108° (center-of-mass system) shows a pronounced hump in the backward hemisphere. The backward hemisphere contains 35.6% of the events. The differential cross section at 0°, $d\sigma^-(0)/\delta\Omega$, extrapolated from the curve is 15 ± 4 mb/sterad. Cool, Piccioni, and Clark[19] give a value of 9.4 (center-of-mass system) on the basis of a 46-mb total cross section. Adjustment of the imaginary part of the forward-scattering amplitude for the larger total cross section of 53.3 mb yields a prediction of 12.6 mb for the elastic differential cross section at 0°.

Table IV

Phenomenological classification

Reaction	No. of events	Fraction of total events	Cross section (mb)
Zero-prong	255 ± 9	0.176 ± 0.006	9.4 ± 0.3
Two-prong	1182 ± 36*	0.814 ± 0.024	43.4 ± 1.3
Four-prong	12 ± 2	0.008 ± 0.001	0.4 ± 0.001
Six-prong	0	0	0
Associated production	3 ± 1	0.002 ± 0.001	0.1 ± 0.001

*Includes 22 ± 5 events in the interval $1 \geq \cos \theta^*_\pi \geq 0.95$ elastic differential cross section, Fig. 18.

Table V

Elastic and single-pion production

Reaction	No. of events analyzed	Fraction of analyzed events	Cross section (mb)
Elastic	261	0.483	21.0 ± 1.1
$\pi^- + p + \pi^0$	80	0.148	6.4
$\pi^- + \pi^+ + n$	199	0.369	16.0
All other interactions	—	—	9.9
		Total cross section =	53.3 ± 2.4

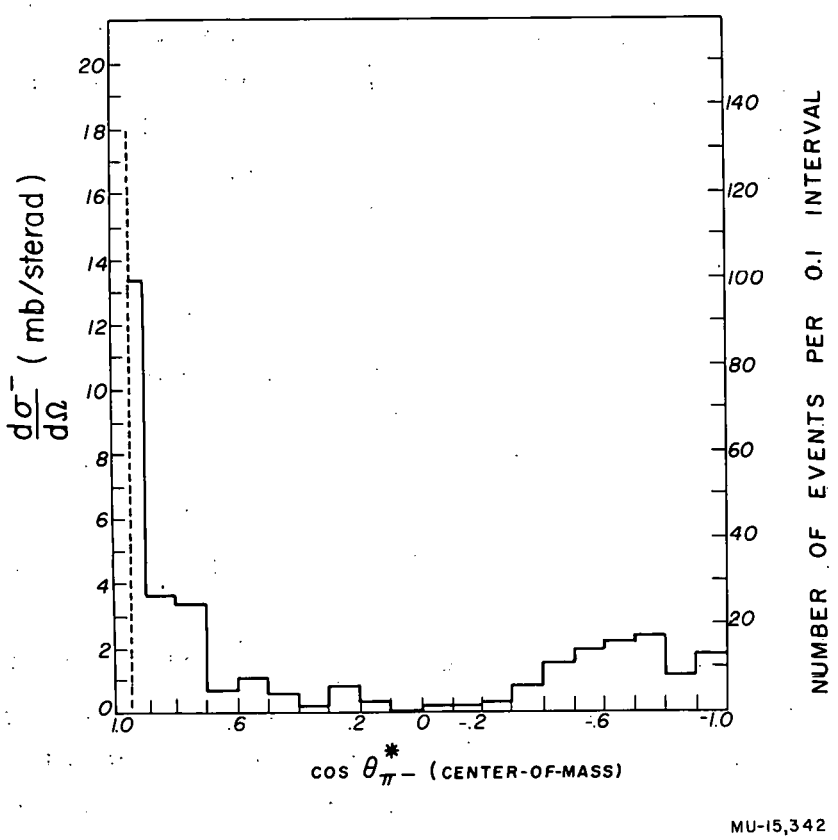

Fig. 18. Elastic π-p differential cross section at 0.939 Bev/c. Events corresponding to scattering of less than 18° in the center-of-mass system are omitted.

C. Distribution of Charged Particles in Single-Pion Production

The momentum distributions of the π^- and proton from $\pi^- + p \rightarrow \pi^- + p + \pi^0$ reactions are given in Fig. 19. The momentum distributions are compared with those predicted by phase-space considerations. The average momentum of the observed π^- is somewhat higher than the average value predicted by phase-space arguments, and are consistent with the momentum distribution anticipated from the isobar model.[10]

In Fig. 20, the momentum histograms of the charged pions from the reaction $\pi^- + p \rightarrow \pi^- + \pi^+ + n$ are drawn. Again the momentum distributions are compared with the phase-space distributions. A marked departure well outside statistics is seen; the π^+ peaks at a momentum of 125 Mev/c greater than center momentum of the π^- distribution.

No attempt was made to identify multiple-pion-production events during this experiment. The number of four-prong events observed ($0.8 \pm 0.1\%$ of total events) indicates that pion multiplicities were infrequent at this value of incident π^- momentum. The single-pion-production events analyzed in this experiment provide a reference point for analysis of single-and multiple-pion production at higher values of momenta, specifically the 1.12 and 1.24 Bev/c data now in the initial stages of analysis.

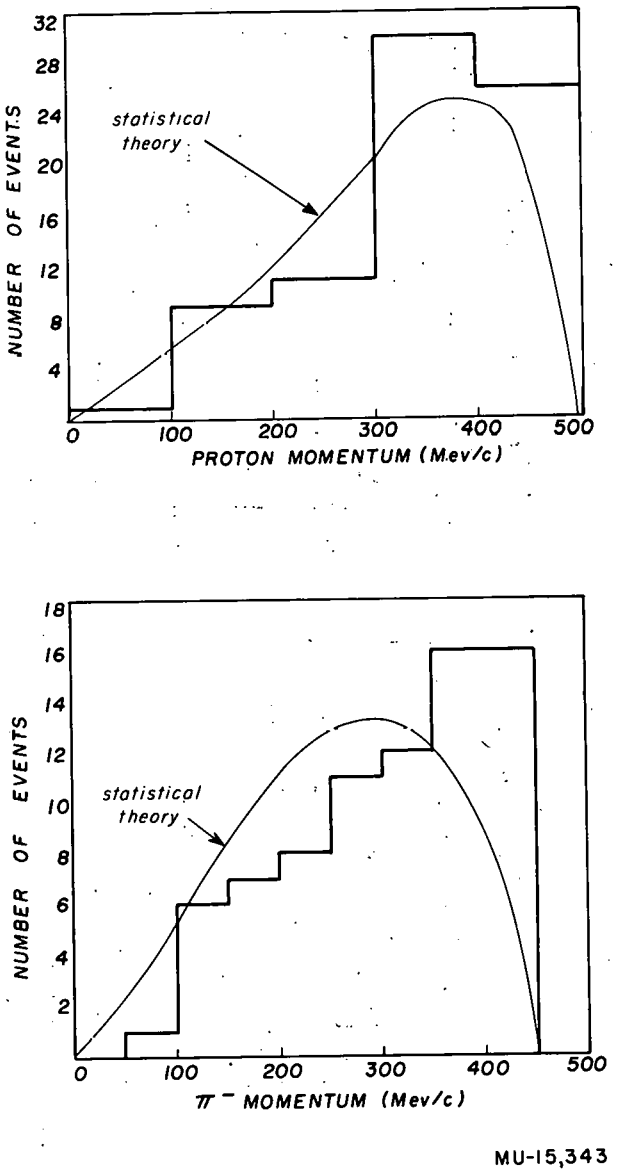

Fig. 19. The momentum distributions of the protons and π^-'s from the $\pi^- + p \rightarrow \pi^- + p + \pi^0$ reaction. Expected phase-space distributions are shown for comparison.

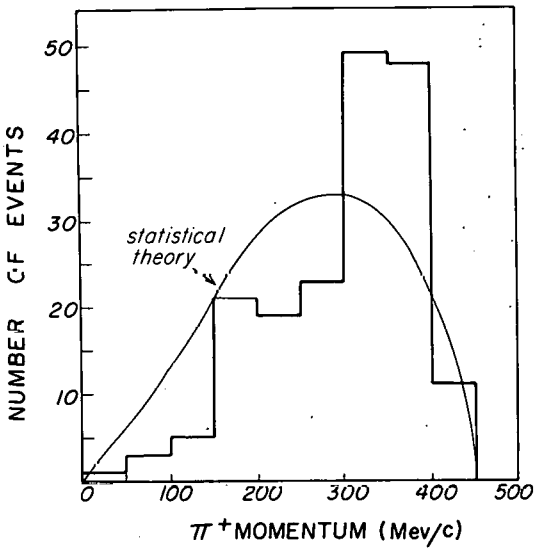

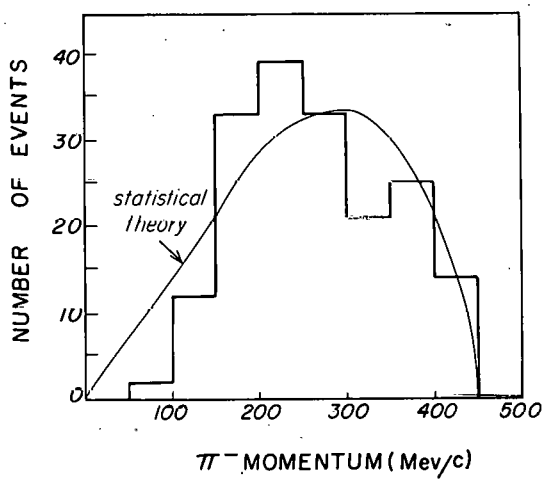

MU-15,344

Fig. 20. The momentum distribution of π's from the $\pi^- + p \rightarrow \pi^- + \pi^+ + n$ reaction. Phase-space distributions are shown.

ACKNOWLEDGMENTS

I wish to express my appreciation to Dr. Luis W. Alvarez, head of the Hydrogen Bubble Chamber Group at UCRL, for his continued interest and encouragement; to Dr. Bruce H. McCormick for his guidance and generous help throughout the entire experiment; to Dr. Frank Solmitz for his suggestions during the analysis; and finally to the bubble-chamber film-scanning group.

This work was done under the joint auspices of the United States Naval Postgraduate School and the United States Atomic Energy Commission.

REFERENCES

1. Fowler, Shutt, Thorndike, and Whittemore, Phys. Rev. 91, 1287 (1953).
2. Budde, Chrétien, Leitner, Samios, Schwartz, and Steinberger, Phys. Rev. 103, 1827 (1956).
3. L. B. Leipuner and R. K. Adair, Phys. Rev. 109, 1358 (1958).
4. Eisberg, Fowler, Lea, Shephard, Shutt, Thorndike, and Whittemore, Phys. Rev. 97, 797 (1955).
5. Walker, Hushfar, and Shephard, Phys. Rev. 104, 526 (1956).
6. W. D. Walker and J. Crussard, Phys. Rev. 98, 1416 (1955).
7. J. Leitner, π^--p Scattering at 1.44 Bev (thesis) NEVIS 28, Jan. 1957.
8. A. R. Erwin, Jr., and J. K. Kopp, Phys. Rev. 109, 1364 (1958).
9. Crawford, Cresti, Good, Gottstein, Lyman, Solmitz, Stevenson, and Ticho, Phys. Rev. 106, 167 (1957).
10. S. J. Lindenbaum and R. M. Sternheimer, Phys. Rev. 106, 1107 (1957).
11. G. Clark, Jr. and W. F. Diehl, Range-Energy Relation for Liquid-Hydrogen Bubble Chambers (M. S. Thesis), UCRL-3789, May 1957.
12. Harold Ticho, Proc. Am. Phys. Soc. Meet., Boulder, Colo., 1957, Paper L-3.
13. Bruce H. McCormick, UCRL Eng. Note 4320-60, M-5 (1957) (unpublished).
14. Marcello Cresti, UCRL Eng. Note 4312-07, M-37 (1957) (unpublished).
15. M. Lynn Stevenson, UCRL (private communication).
16. Frank T. Solmitz, UCRL Eng. Note 4320-60, M-6 (1957) (unpublished).
17. Horace Taft, UCRL Eng. Note 4320-60, M-7 (1957) (unpublished).
18. Frank Crawford, UCRL Eng. Note 4310-03, LA-16 (1958) (unpublished).
19. Cool, Piccioni, and Clark, Phys. Rev. 103, 1082 (1956).